

*Electronic Supplementary Information for*

Tuning the adsorption behaviors of non-noble electrocatalysts to  
boost valorization of 5-hydroxymethylfurfural

Yunpeng He, Botao Zhu,\* Feng Wang, Jie Xiong, Muhammad Awais Akram, Lai  
Feng\*

*College of Energy, Soochow Institute for Energy and Materials Innovation, Key  
Laboratory of Core Technology of High Specific Energy Battery and Key Materials  
for Petroleum and Chemical Industry, Soochow University, Suzhou 215006, China.*

## ***1. Experimental details.***

### *1.1 Product analysis.*

To qualitatively estimate the HMFOR products after chronoamperometry test at 1.52  $V_{\text{RHE}}$ , the products were separated by adding HCl (2 M) into the electrolyte to pH= 1, and washed by DI Water, followed by vacuum dry. The HMFOR separated products were dissolved in  $D_2O$  for UV-Vis absorption measurement and  $^1H$  NMR analysis using methanol ( $CH_3OH$ ) as the internal reference. To separate HMFRR products after chronoamperometry test at -0.7  $V_{\text{RHE}}$  or various working potentials, 9 mL ethyl acetate was used to extract products from 3 mL electrolyte. Afterwards, the extract was dried by anhydrous sodium sulfate and filtered, and analyzed by using GC-mass with flame-ionization detection (FID), electron capture detection (ECD) and mass spectrometry detection (MSD).

To analyze the HMFOR products after the chronoamperometry (CA) test at 1.52  $V_{\text{RHE}}$ , 10  $\mu\text{L}$  electrolyte was subjected for HPLC analysis by using aqueous solution containing 30% methanol and 5 mM ammonium formate as mobile phase with a flow rate of 0.6  $\text{mL min}^{-1}$  at 40  $^{\circ}\text{C}$ , and a UV detector with  $\lambda = 265$  nm. Alternatively, the products of HMFRR at -0.7  $V_{\text{RHE}}$  were analyzed by HPLC using aqueous solution containing 10% methanol and 5 mM ammonium formate as mobile phase with a flow rate of 0.6  $\text{mL min}^{-1}$  at 40  $^{\circ}\text{C}$ , and a UV detector with  $\lambda = 220$  nm. Both the HMFOR and HMFRR products were quantitatively determined by the external standard method based on the standard samples including HMF, HMFCA, DFF, FFCA, FDCA, and BHMF.

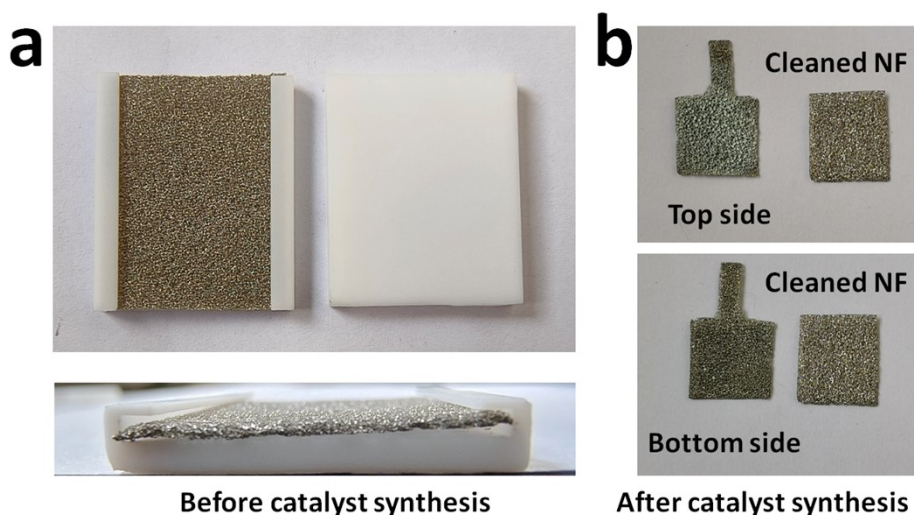


**Figure S1.** (a) Photos of the cleaned NF with PTFE template for catalyst synthesis; (b) Photos of the catalyst modified NF (top side and bottom side) along with a cleaned NF (with random size) as reference. It is clearly seen that the as-synthesized catalyst is uniformly distributed on the top side of NF and negligible catalyst on the bottom side.

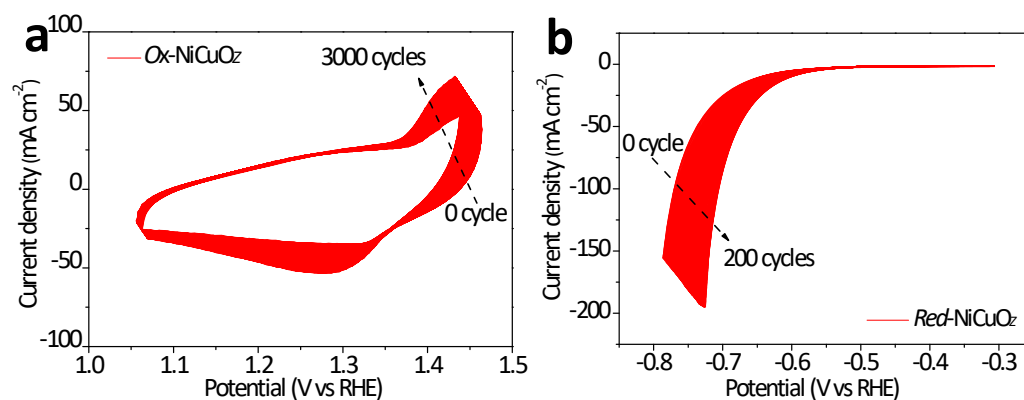


**Figure S2.** (a) Multiple CV sweeps of anode to achieve reconstructed catalyst Ox-NiCuO<sub>z</sub> under HMFOR conditions and (b) those of cathode to achieve Red-NiCuO<sub>z</sub> under HMFRR conditions.

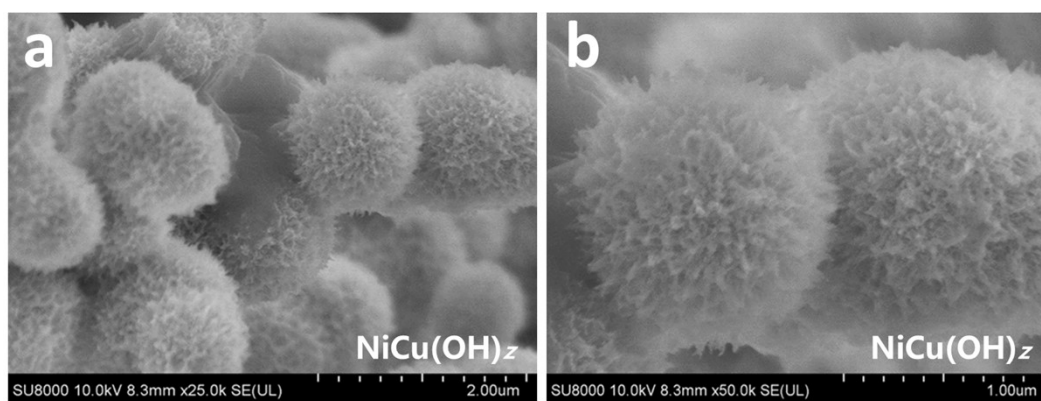


**Figure S3.** (a,b) SEM images of  $\text{NiCu(OH)}_z$ .

**Table S1.** ICP analysis results of various catalysts.<sup>a</sup>

Catalyst	Ni/Cu molar ratio	Note
$\text{NiCu(OH)}_z$	2.8/1	Free-standing powder sample.
$\text{NiCuO}_z$	2.5/1	Free-standing powder sample
$O_x\text{-NiCuO}_z$	5/1	Sample synthesized on Ti foam
$O_x\text{-NiCu(OH)}_z$	5/1	Sample synthesized on Ti foam
$Red\text{-NiCuO}_z$	5/1	Sample synthesized on Ti foam

<sup>a</sup>All catalysts were dissolved in aqua regia and diluted as ICP samples.



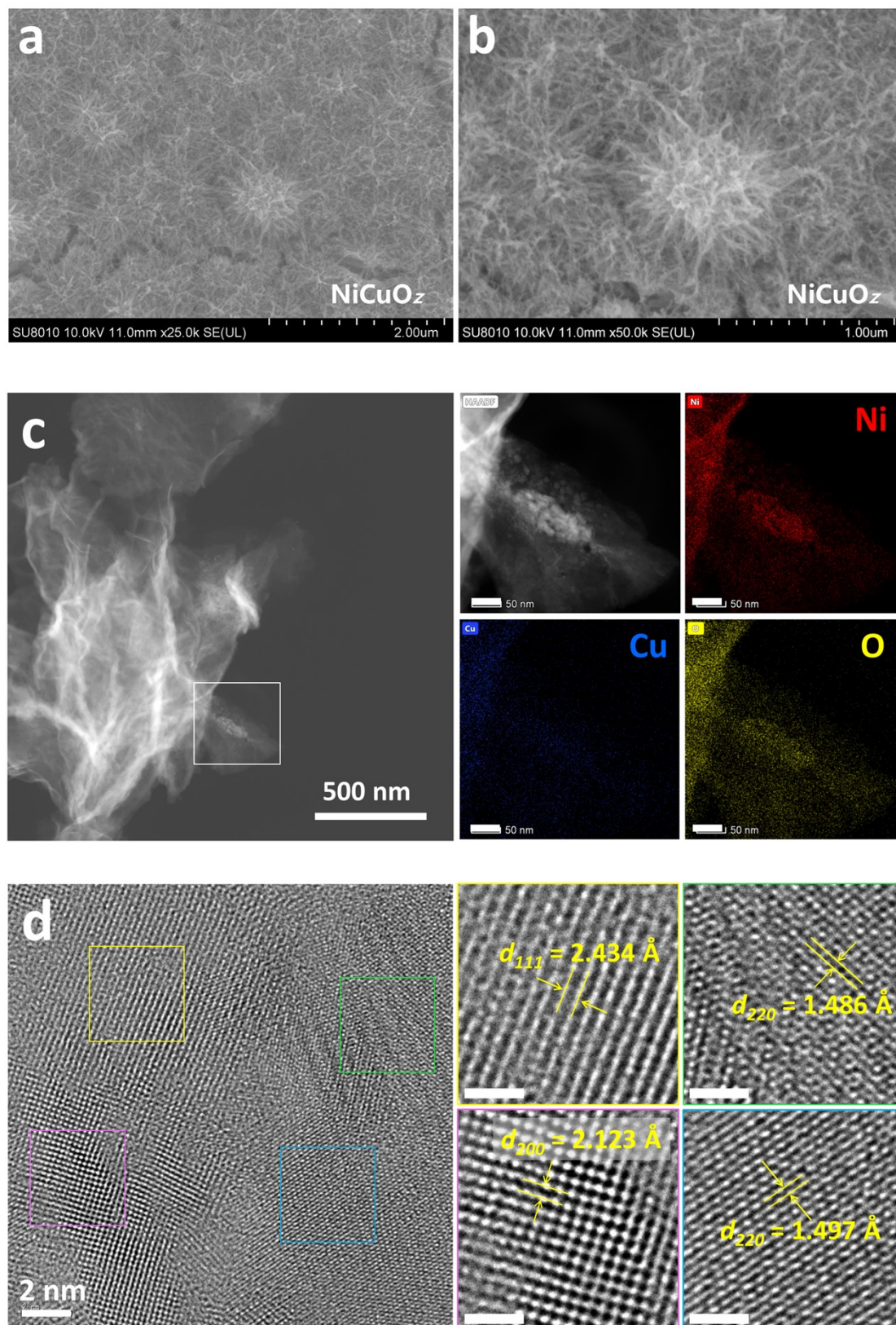


**Figure S4.** (a,b) SEM images of NiCuO<sub>z</sub>. (c) HAADF image of NiCuO<sub>z</sub> and corresponding elemental mapping images with the scale bar of 50 nm. (d) HR-TEM image of NiCuO<sub>z</sub> and magnified images (with a scale bar of 1 nm) of local regions.

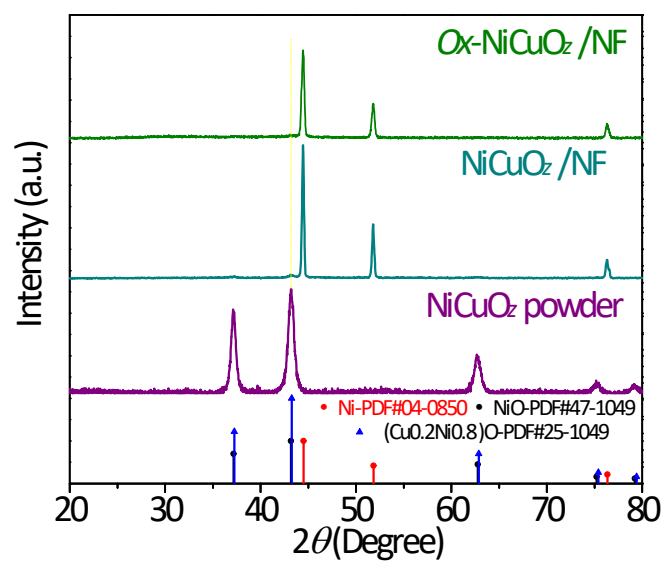


**Figure S5.** XRD patterns of NiCuO<sub>z</sub> samples synthesized with and without NF.

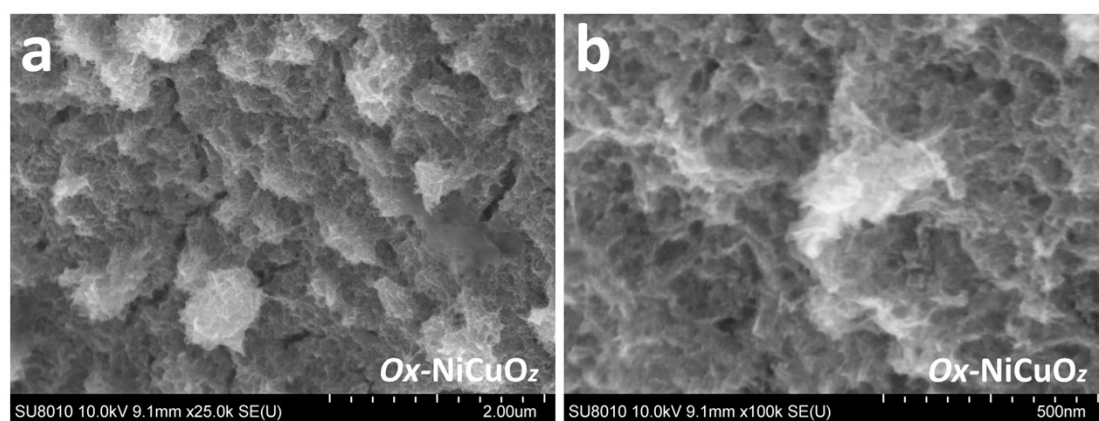


**Figure S6.** (a,b) SEM images of Ox-NiCuO<sub>z</sub>.

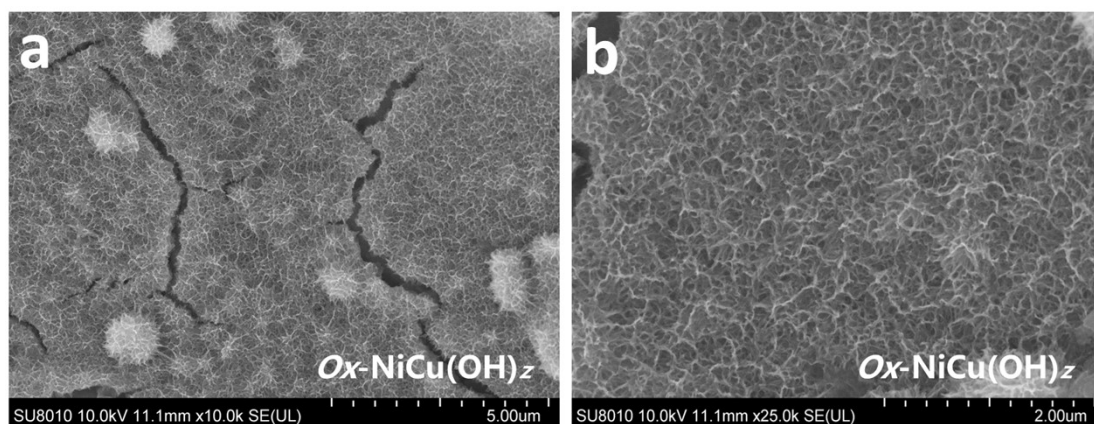


**Figure S7.** (a,b) SEM images of Ox-NiCu(OH)<sub>z</sub>.



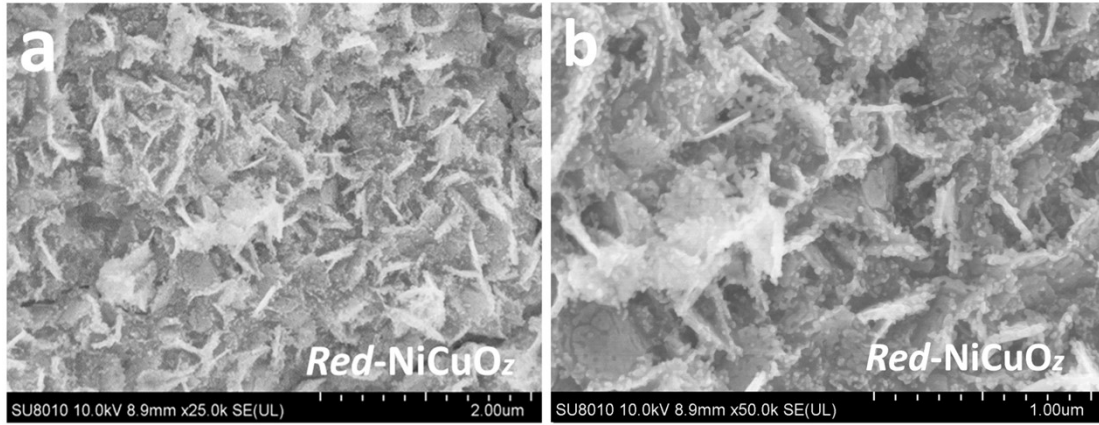


Figure S8. (a,b) SEM images of Red-NiCuO<sub>z</sub>.

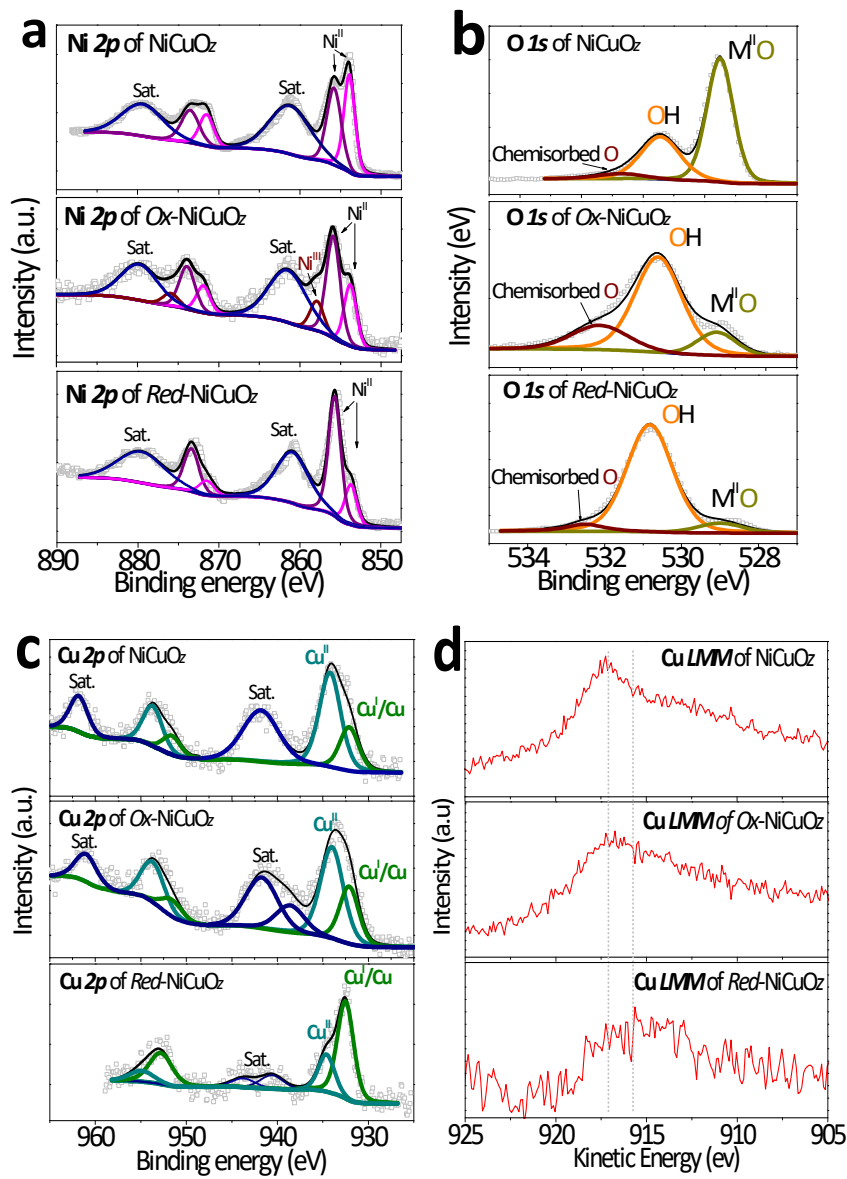
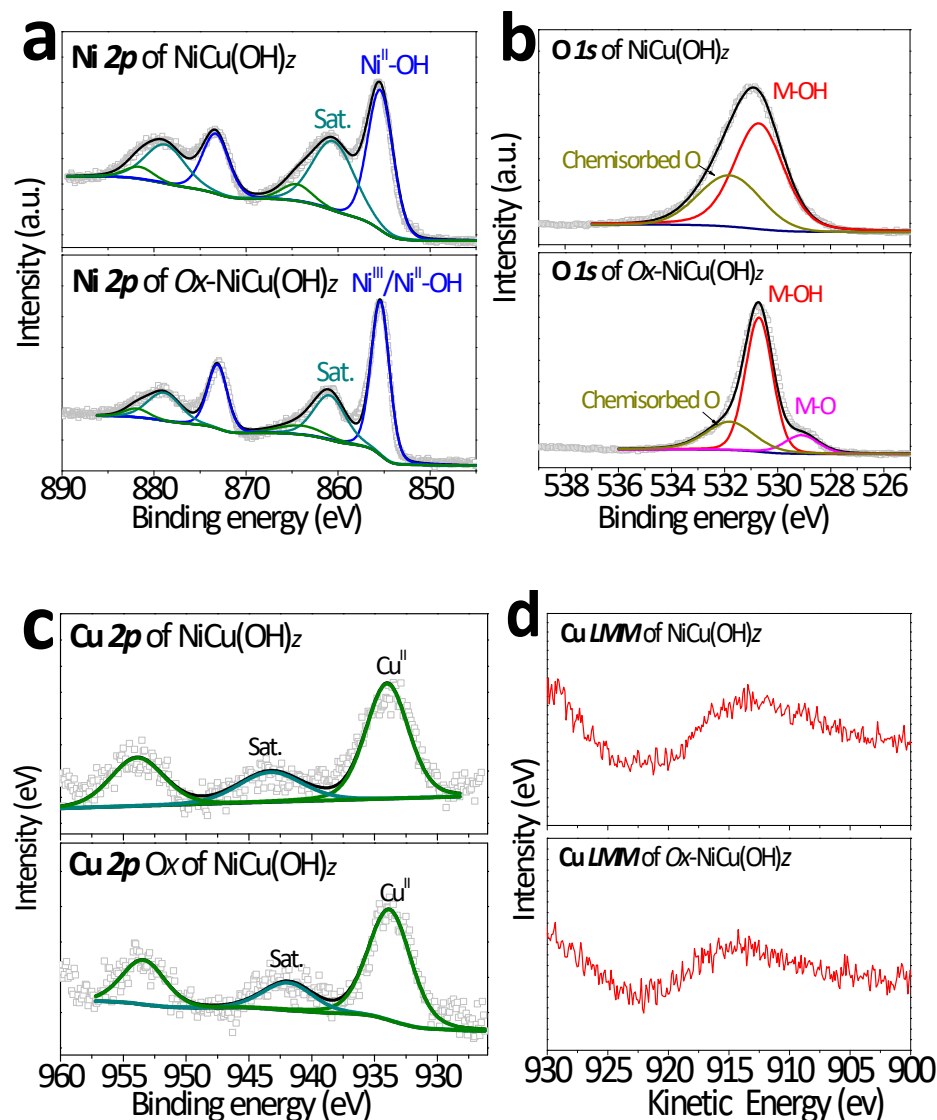


Figure S9. XPS spectra of NiCuO<sub>z</sub>, Ox-NiCuO<sub>z</sub> and Red-NiCuO<sub>z</sub>. (a) Ni 2p, (b) O 1s (c) Cu 2p and (d) Cu-LMM.

Note: In **Figure S9a**, the pristine NiCuO<sub>z</sub> shows the peaks at 853.8/855.8 eV and 861.4 eV, which can be assigned to the multi-split of Ni 2p<sub>3/2</sub> of Ni<sup>II</sup> and corresponding satellite.<sup>1,2</sup> The Ox-NiCuO<sub>z</sub> shows the appearance of a new peak at 857.0 eV indexed to Ni<sup>III</sup>, indicating the formation of Ni<sup>III</sup>OOH on the catalyst surface due to anodic reconstruction. As for the Red-NiCuO<sub>z</sub>, the Ni 2p<sub>3/2</sub> peaks can be again ascribed to Ni<sup>II</sup>. In **Figure S9b**, the pristine NiCuO<sub>z</sub> displays a major O 1s peak at 529.8 eV, corresponding to the oxygen of Ni<sup>II</sup>O and Cu<sup>II</sup>O. Whereas, Ox-NiCuO<sub>z</sub> and Red-NiCuO<sub>z</sub> each presents a major peak at 531.5 ~ 531.7 eV, which combined with the Ni 2p spectra indicate the presence of Ni<sup>III</sup>OOH and Ni(OH)<sub>2</sub> on the respective catalyst surface. **Figures S9c,d** suggest that the NiCuO<sub>z</sub> and Ox-NiCuO<sub>z</sub> involve more Cu<sup>II</sup> than Cu<sup>I</sup>, while Red-NiCuO<sub>z</sub> has more Cu<sup>I</sup> than Cu<sup>II</sup>.

#### References in Note of **Figure S9**.

- [1]. Yang, Y.; Xu, D.; Zhang, B.; Xue, Z.; & Mu, T. Substrate molecule adsorption energy: an Activity Descriptor for Electrochemical Oxidation of 5-Hydroxymethylfurfural (HMF). *Chem. Eng. J.* **2022**, *433*, 133842.
- [2]. Choi, S.; Balamurugan, M.; Lee, K.-G.; Cho, K. H.; Park, S.; Seo, H.; and Nam, K. T. Mechanistic Investigation of Biomass Oxidation Using Nickel Oxide Nanoparticles in a CO<sub>2</sub>-Saturated Electrolyte for Paired Electrolysis. *J. Phys. Chem. Lett.* **2020**, *11*, 2941-2948.



**Figure S10.** XPS spectra of NiCu(OH)<sub>2</sub> and Ox-NiCu(OH)<sub>2</sub>. (a) Ni 2p, (b) O 1s, (c) Cu 2p and (d) Cu-LMM.

Note: As shown in **Figure S10a**, both samples including NiCu(OH)<sub>2</sub> and Ox-NiCu(OH)<sub>2</sub> show a photoelectron peak of 2p<sub>3/2</sub> at 855.4 ± 0.1 eV, which indicates the presence of Ni<sup>II</sup>-OH or Ni<sup>III</sup>-OOH/Ni<sup>II</sup>-OH on the sample surface. However, further peak deconvolution will be very artificial due to the very close binding energies of Ni<sup>III</sup>-OOH and Ni<sup>II</sup>-OH. Nevertheless, it is noted that their satellite peaks at around 861 eV are obviously varied in the relative peak area to that of Ni 2p<sub>3/2</sub>. The ratio of Ni 2p<sub>3/2</sub>/satellite is 1.0 for NiCu(OH)<sub>2</sub>, while that is 1.5 for Ox-NiCu(OH)<sub>2</sub>. Based on the literature reports,<sup>1,2</sup> “shakeup satellite peaks are observed only for the paramagnetic nickel ion (example octahedral nickel(II) or tetrahedral Ni(II))”. So, satellite peaks shall be observed for the Ni<sup>II</sup>-OH but not for the diamagnetic Ni<sup>III</sup>-OOH. The reduced satellite peak of Ox-NiCu(OH)<sub>2</sub> relative to that of NiCu(OH)<sub>2</sub> indicates there is Ni<sup>III</sup>-OOH partially covered on the surface of Ox-NiCu(OH)<sub>2</sub>, in line with their color difference (i.e., black for Ox-NiCu(OH)<sub>2</sub> and light gray for

NiCu(OH)<sub>2</sub>). In addition, the O 1s spectrum of Ox-NiCu(OH)<sub>2</sub> displays three peaks at 529.1, 530.7 and 531.8 eV, belonging to the M-O, M-OH and adsorbed H<sub>2</sub>O or O<sub>2</sub>, indicating again the presence of Ni<sup>III</sup>-OOH species.<sup>3</sup>

Meanwhile, both catalysts show similar O1s, Cu2p and Cu-LMM spectra, suggesting the oxygen of hydroxide group and Cu<sup>II</sup> are major components.

References in Note of Figure S10.

- [1]. J. Rajpurohit, P. Shukla, P. Kumar, C. Das, S. Vaidya, M. Sundararajan, M. Shanmugam, and M. Shanmugam. Stabilizing Terminal Ni(III)–Hydroxide Complex Using NNN-Pincer Ligands: Synthesis and Characterization. *Inorg. Chem.* **2019**, *58*, 6257-6267.
- [2]. A. Rosencwaig, G. K. Wertheim, and H. J. Guggenheim, Origins of Satellites on Inner-Shell Photoelectron Spectra. *Phys. Rev. Lett.* **1971**, *27*, 479-481.
- [3]. Y. Huang, X. Pang, J. Cui, Z. Huang, G. Wang, H. Zhao, H. Bai, and W. Fan, Strengthening the Stability of the Reconstructed NiOOH Phase for 5-Hydroxymethylfurfural Oxidation. *Inorg. Chem.* **2023**, *62*, 6499-6509

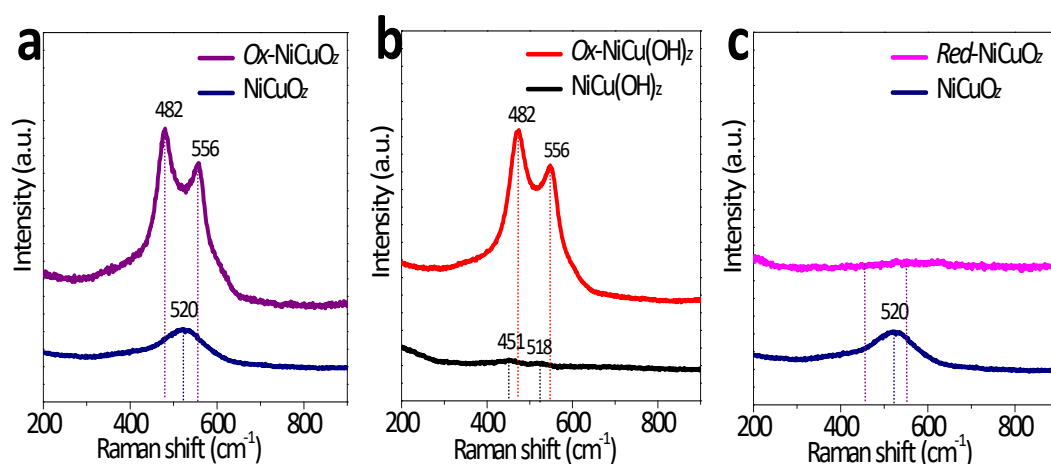


**Figure S11.** (a) Raman spectra of NiCuO<sub>2</sub> and Ox-NiCuO<sub>2</sub>; (b) NiCu(OH)<sub>2</sub> and Ox-NiCu(OH)<sub>2</sub>; (c) NiCuO<sub>2</sub> and Red-NiCuO<sub>2</sub>.

Note: For Ox-NiCuO<sub>2</sub> and Ox-NiCu(OH)<sub>2</sub>, the feature bands of Ni<sup>III</sup>OOH are evident, suggesting the accumulation of Ni<sup>III</sup>OOH during the anodic reconstructions. As for Red-NiCuO<sub>2</sub>, the feature band of Ni<sup>II</sup>O is almost negligible, indicating the possible formation of Ni<sup>II</sup>(OH)<sub>2</sub> with more featureless Raman bands.

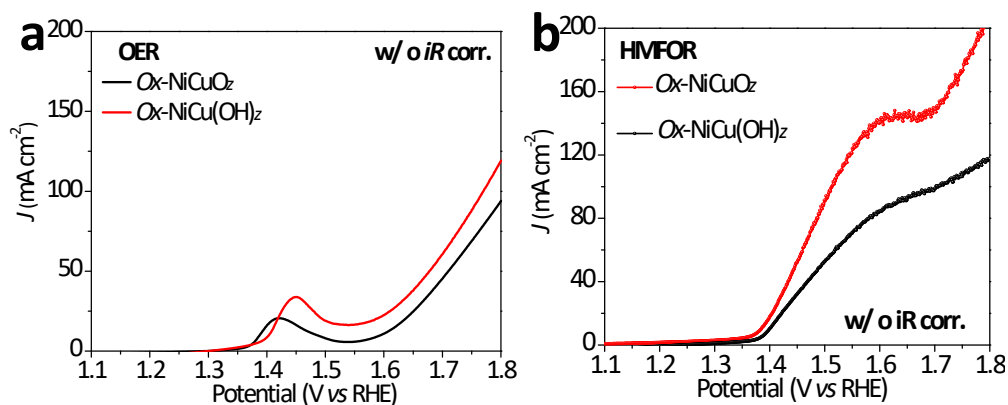


**Figure S12.** LSV curves (without  $iR$  correction and a scan rate of  $5 \text{ mV s}^{-1}$ ) of the  $\text{Ox-NiCuO}_2$  and  $\text{Ox-NiCu(OH)}_2$  in 1 M KOH (a) without and (b) with 10 mM HMF, where the  $R_s$  was measured as  $0.7 \sim 0.9 \Omega$ .

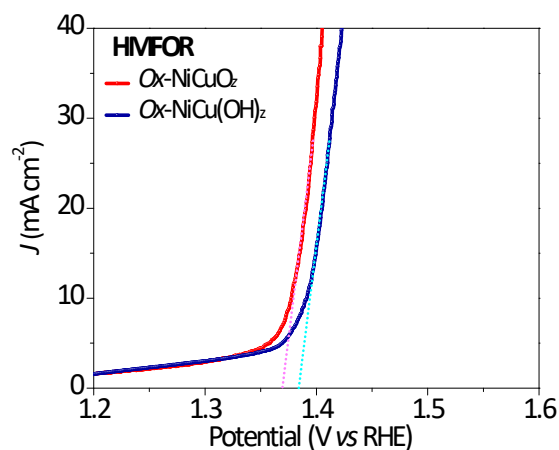


**Figure S13.** The magnified LSV curves (with  $iR$  correction) about the region of onset potential of HMFOR over  $\text{Ox-NiCuO}_2$  and  $\text{Ox-NiCu(OH)}_2$  corresponding to **Figure 3a**.

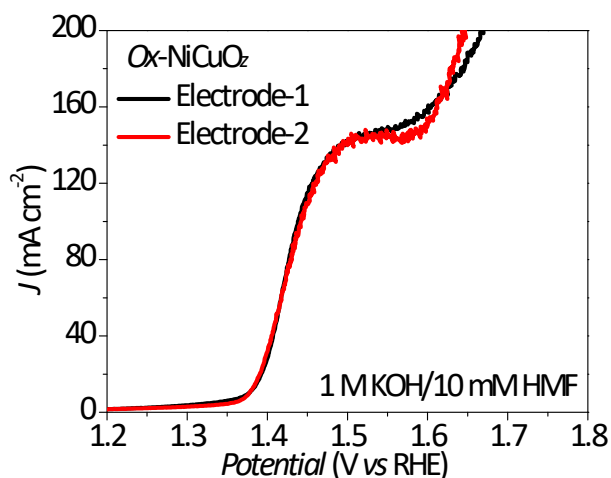


**Figure S14.** LSV curves of two individual  $\text{Ox-NiCuO}_2$  electrodes in 1 M KOH with 10 mM HMF at a scan rate of  $5 \text{ mV s}^{-1}$ .

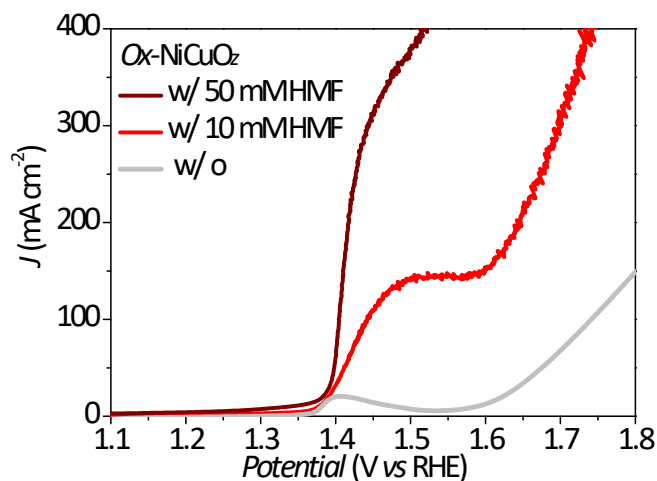


**Figure S15.** LSV curves of  $Ox-NiCuO_2$  in 1 M KOH without and with 10 mM/50 mM HMF at a scan rate of  $5 \text{ mV s}^{-1}$ .

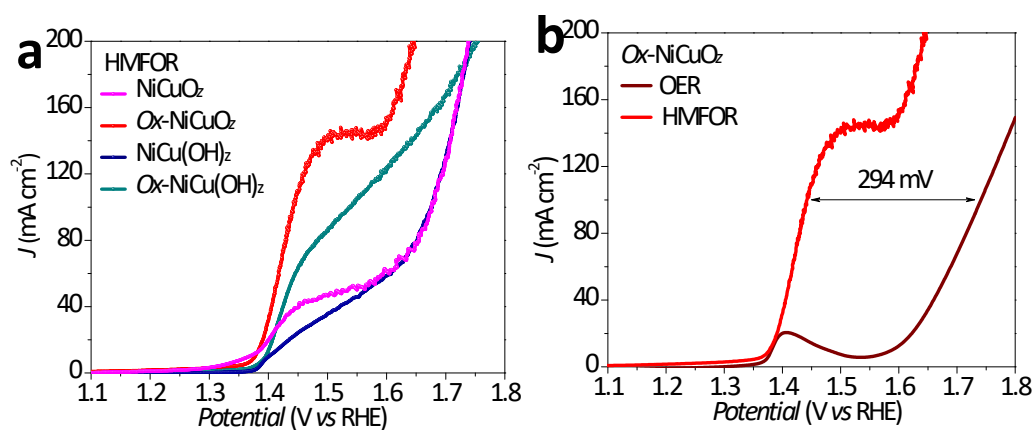


**Figure S16.** (a) LSV curves of  $NiCuO_2$ ,  $Ox-NiCuO_2$ ,  $NiCu(OH)_2$  and  $Ox-NiCu(OH)_2$  in 1 M KOH with 10 mM HMF at a scan rate of  $5 \text{ mV s}^{-1}$ . (b) LSV curves of  $Ox-NiCuO_2$  in 1 M KOH without and with 10 mM HMF at a scan rate of  $5 \text{ mV s}^{-1}$ .

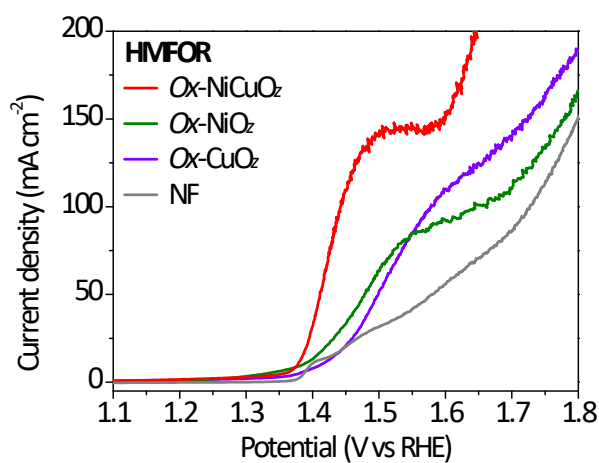


**Figure S17.** LSV curves (with  $iR$  compensation and a scan rate of  $5 \text{ mV s}^{-1}$ ) of the  $Ox-NiCuO_2$  and  $Ox-NiO_2$ ,  $Ox-CuO_2$ , nickel foam (NF).



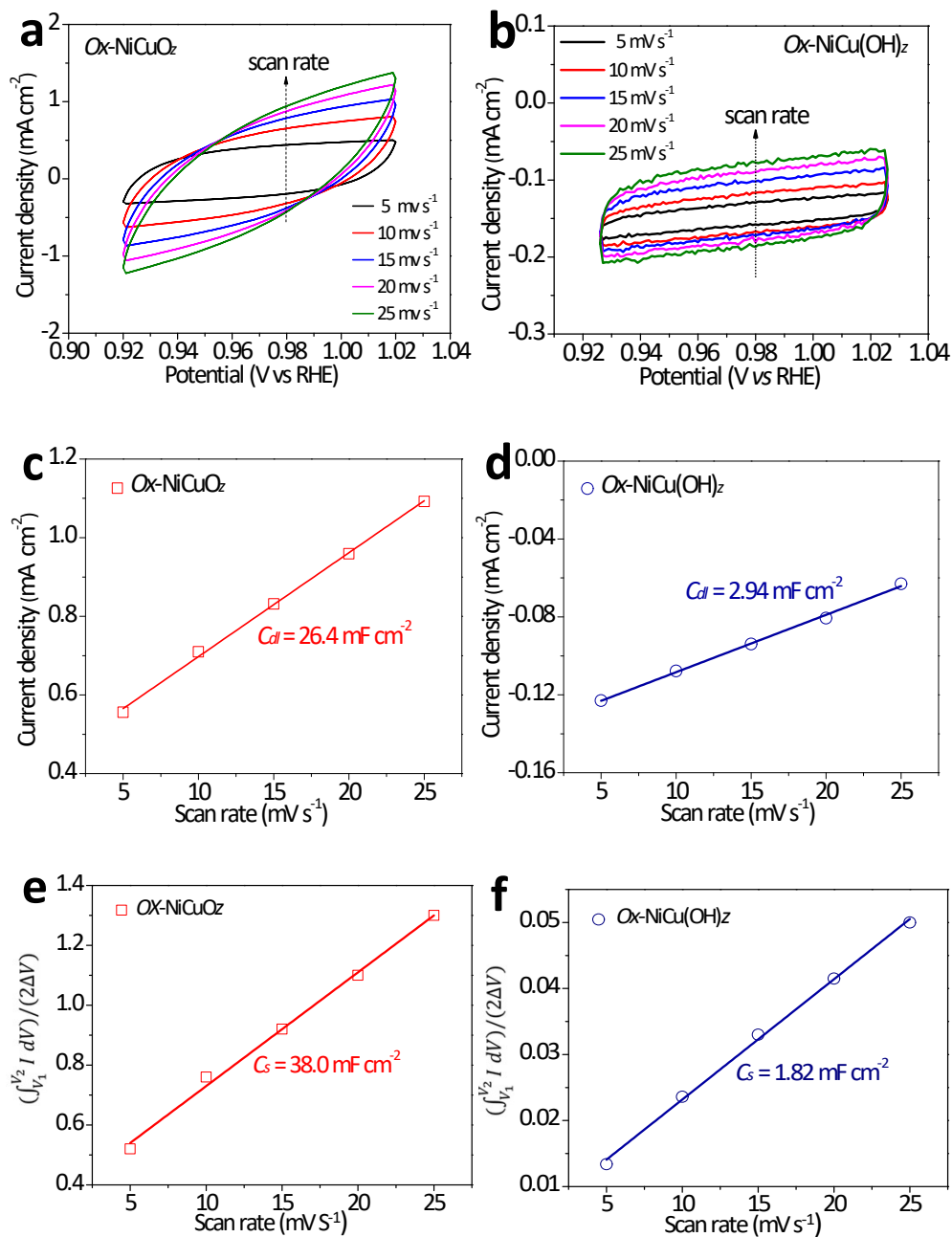


**Figure S18.** CV curves (in the non-Faradaic range), plots of current density or

$$\int_{V_1}^{V_2} I dV$$

$2\Delta V$  versus scan rate ( $\nu$ ) of (a,c,e) Ox-NiCuO<sub>z</sub> and (b,d,f) Ox-NiCu(OH)<sub>z</sub>.

Note: ECSA could be determined based on the equation of  $ECSA = C_{dl}/C_s$ , where  $C_{dl}$  and  $C_s$  refer to double-layer capacitance and specific capacitance, respectively. As the  $C_s$  may change depending on the composition of the electrocatalyst, it is determined from independent experiment utilizing known-area electrode according to the following equation:

$$C_s = \frac{\int_{V_1}^{V_2} I dV}{2\nu \Delta V}$$

$$\int_{V_1}^{V_2} I dV$$

Where  $\int_{V_1}^{V_2} I dV$  is the area of CVs,  $\nu$  is scan rate ( $\text{V s}^{-1}$ ), and  $\Delta V$  is potential window.

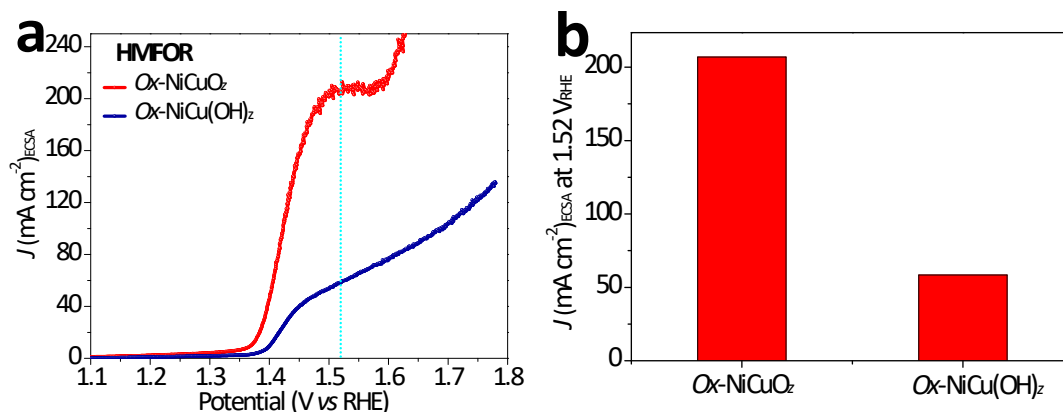
$$\int_{V_1}^{V_2} I dV$$

Thus,  $C_s$  is the slope of scan rate and  $\frac{\int_{V_1}^{V_2} I dV}{2\Delta V}$  plot.<sup>1</sup>

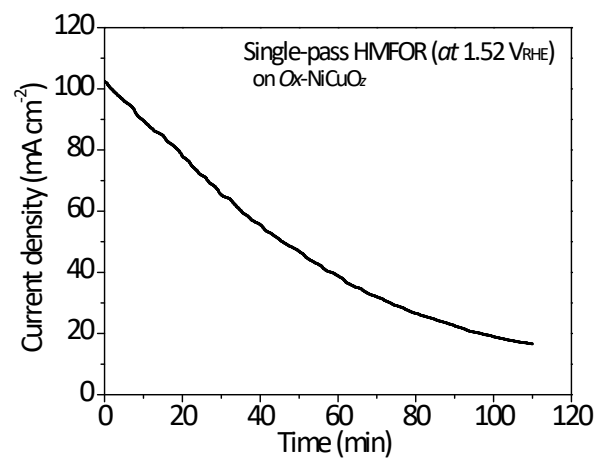
As a result, ECSA could be determined as  $0.695 \text{ cm}^2$  ( $Ox\text{-NiCuO}_2$ ) and  $1.633 \text{ cm}^2$  ( $Ox\text{-NiCu(OH)}_2$ ).

Reference in Note of **Figure S18**.

[1]. Liu, C.; Hirohara, M.; Maekawa, T.; Chang, R.; Hayashi, T.; Chiang, C.-Y. *Appl. Catal. B: Environ.* **2020**, *265*, 118543.



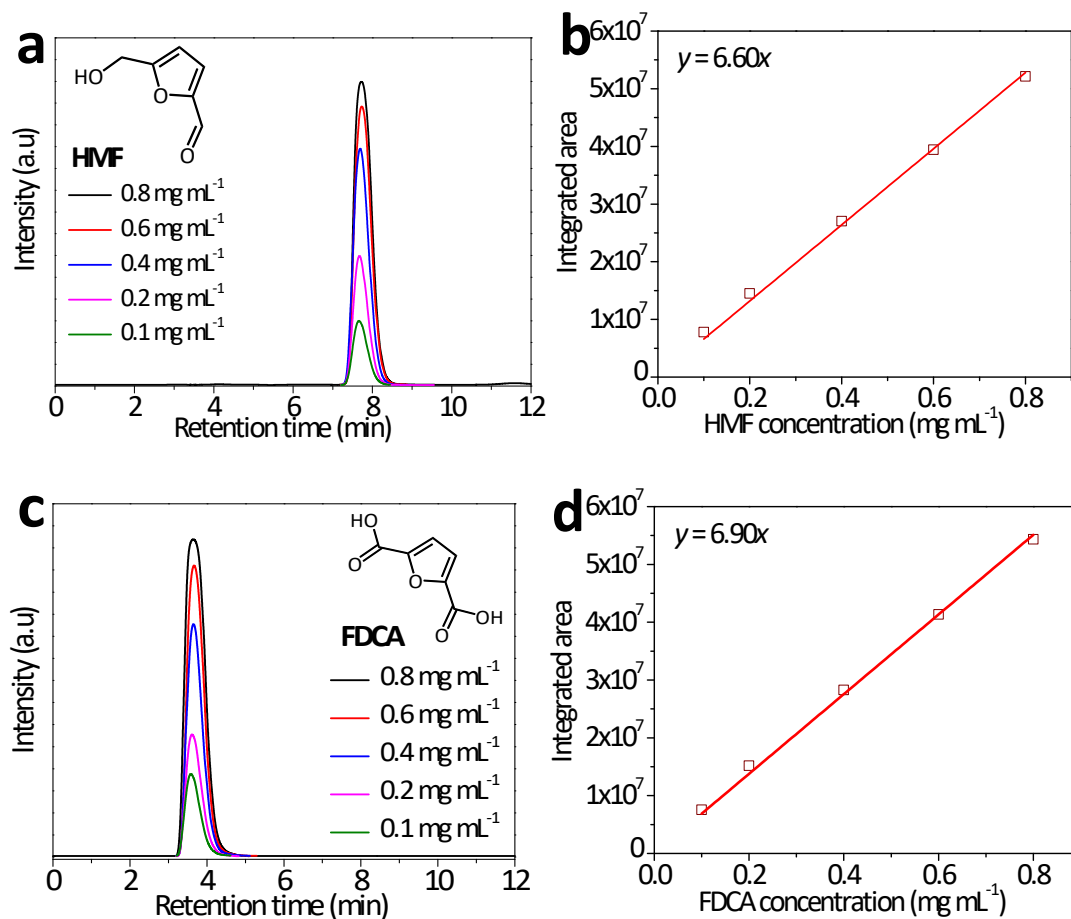
**Figure S19.** (a) LSV curves (with  $iR$  correction and a scan rate of  $5 \text{ mV s}^{-1}$ ) of the  $Ox\text{-NiCuO}_2$  and  $Ox\text{-NiCu(OH)}_2$  with ECSA normalization in 1 M KOH with 10 mM HMF. (b) Comparison between the ECSA normalized current density of HMFOR at  $1.52 \text{ V}_{\text{RHE}}$  of different catalysts.



**Figure S20.** CA profile for a single-pass test over Ox-NiCuO<sub>2</sub> at 1.52 V<sub>RHE</sub>.

**Table S2.** Summary of the data corresponding to **Figure 3c** and **Figure S20**.

Time (min)	Produced FDCA (mmol)	FDCA Yield (%)	Required charge for produced FDCA (C)	Actually passed charge (C)	FE <sub>FDCA</sub> (%)	HMF (mmol)	HMF conv. (%)
10	0.201	35.9	116.30	118.13	98.45	0.339	39.4
20	0.254	45.3	146.79	151.09	97.15	0.294	47.5
30	0.285	50.8	164.77	169.56	97.18	0.241	57.0
40	0.355	63.3	205.28	211.18	97.21	0.186	66.8
50	0.432	77.1	250.06	255.03	98.05	0.119	78.8
60	0.452	80.7	261.48	264.40	98.89	0.105	81.2
70	0.458	81.7	264.89	274.24	96.59	0.086	84.6
80	0.468	83.6	271.04	280.43	96.65	0.061	89.1
90	0.490	87.5	283.73	292.52	97.00	0.055	90.2
100	0.511	91.3	296.07	307.60	96.25	0.039	93.0
110	0.544	97.1	314.78	321.14	98.02	0.014	97.5



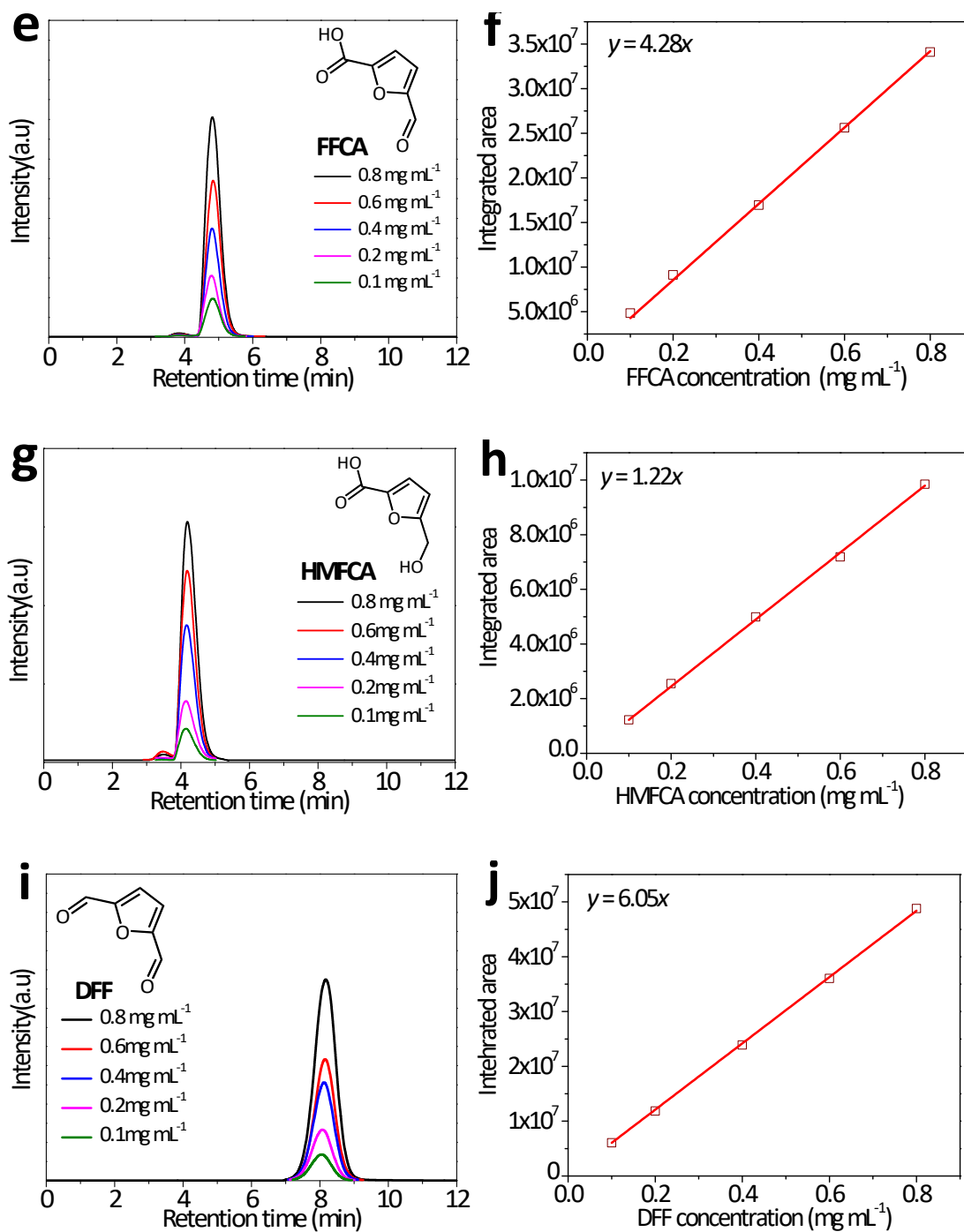


**Figure S21.** HPLC chromatograms (with a monitor of  $\lambda = 265$  nm) and calibration plots of standard samples of (a,b) HMF, (c,d) FDCA, (e,f) FFCA, (g,h) HMFCA and (i,j) DFF.

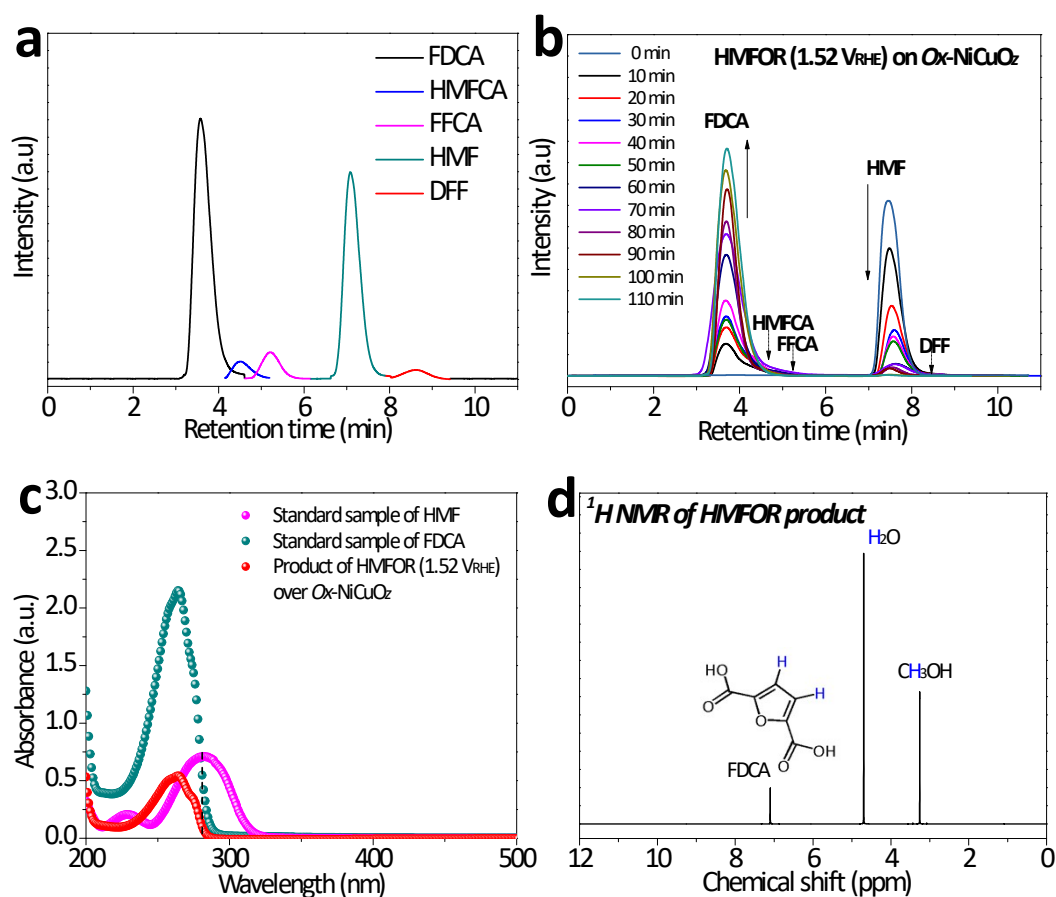


**Figure S22.** (a) Combined HPLC chromatograms of standard samples of HMF, HMFCFA, FFCA, FDCA and DFF. (b) HPLC chromatograms of HMFOR products at 1.52  $V_{RHE}$  over  $Ox-NiCuO_z$  with the increasing of reaction time. (c) UV-Vis absorption spectra of standard samples of HMF, FDCA and the HMFOR products over  $Ox-NiCuO_z$  at 1.52  $V_{RHE}$ . (d)  $^1H$  NMR spectrum of the HMFOR products over  $Ox-NiCuO_z$  at 1.52  $V_{RHE}$ .  $^1H$  NMR (400 MHz,  $D_2O$  with methanol as internal standard):  $\delta = 7.10$  (s, 2H).

Note: Due to the large dead volume in our employed HPLC, the chromatographic peak of FDCA is somewhat overlaid with those of HMFCFA and FFCA, while the peak of HMF is somewhat overlaid with that of DFF. Their peak areas are estimated by using the software packed with HPLC. As the FDCA or HMF peak is much more overwhelming than the HMFCFA/FFCA or DFF peak, the estimation on FDCA or HMF peak area is more precise. On the other hand, as the HMFCFA/FFCA or DFF peak is much smaller, the estimation on their peak areas inevitably results in higher deviation. Nevertheless, their peak areas were estimated using the same method, so the results could reflect their relative contents.

The  $^1H$  NMR signal at  $\delta = 7.10$  ppm corresponds to the CH of FDCA. As no other  $^1H$  signals related to the HMFOR products could be detected,  $^1H$  NMR analysis indicates again that FDCA is the major product of HMFOR.

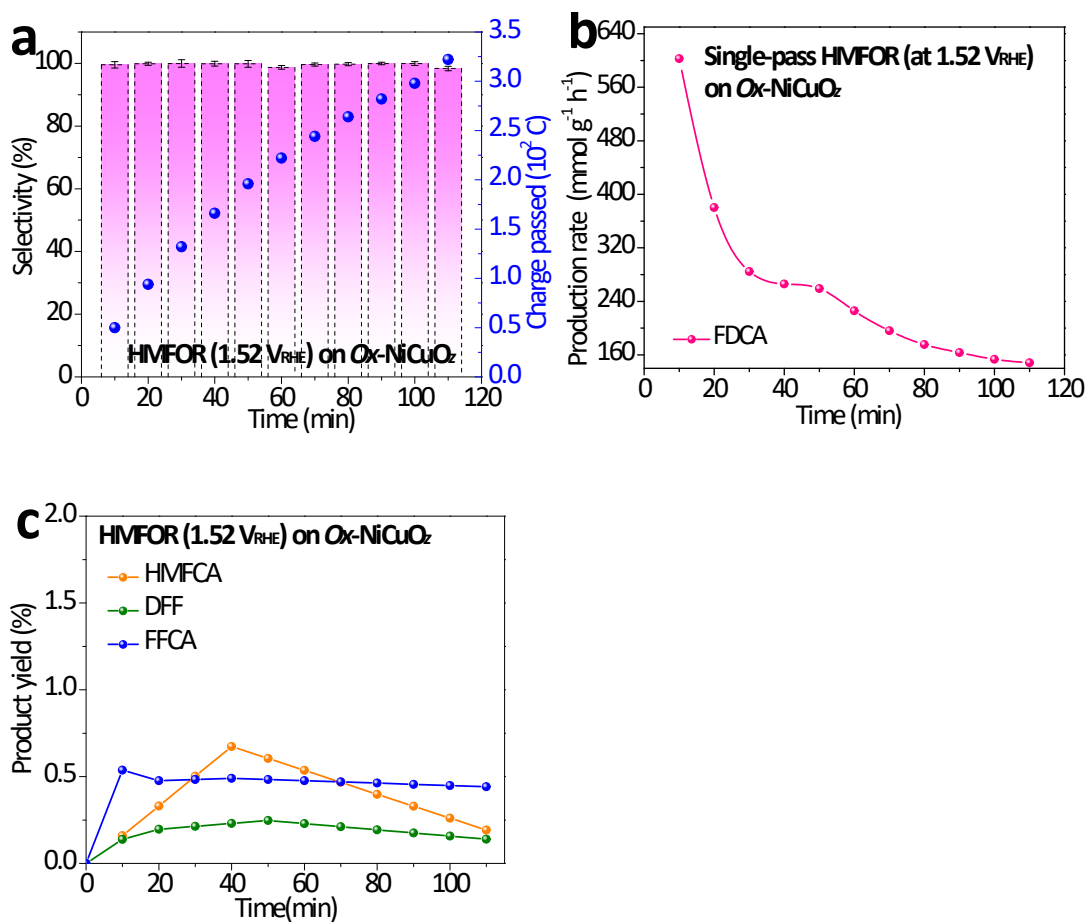


**Figure S23.** (a) Selectivity and (b) product rate of FDCA; (c) product yields of HMFCA, DFF and FFCA calculated for a single-pass chronoamperometric (CA) test over  $O\alpha$ -NiCuO<sub>z</sub> at 1.52  $V_{RHE}$ .

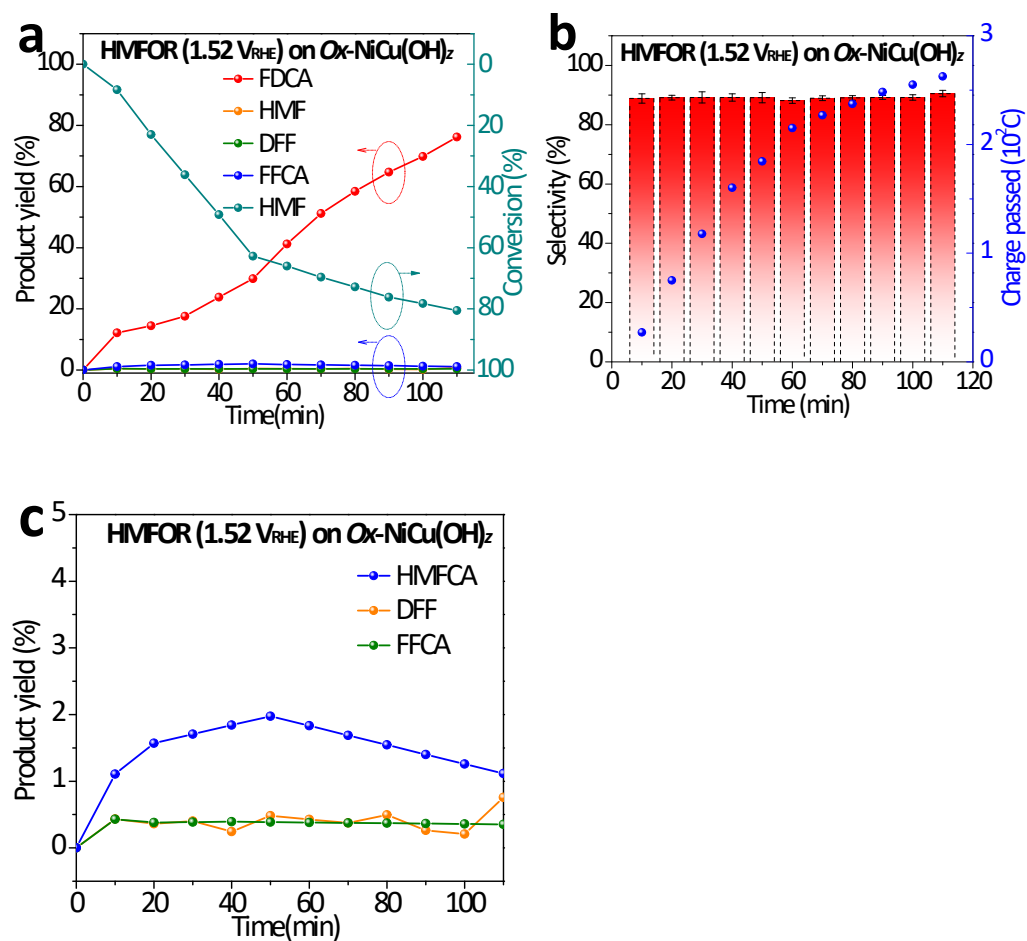


**Figure S24.** (a) Relative change (%) of HMF conversion and product yields during a single-pass chronoamperometric (CA) test over O<sub>x</sub>-NiCu(OH)<sub>z</sub> at 1.52 V<sub>RHE</sub>, (b) corresponding selectivity of FDCA, and (c) product fields of HMFCFA, DFF and FFCA.



**Table S3.** Summary of catalytic performance of Ni-based electrocatalysts towards HMFOR.

Catalyst	Electrolyte	HMF (mM)	E (V <sub>RHE</sub> ) at 20 mA cm <sup>-2</sup>	Optimal E (V <sub>RHE</sub> )	FDCA yield (%)	FE <sub>FDCA</sub> (%)	Ref.
Ox-NiCuO <sub>2</sub>	1.0 M KOH	10	1.39	1.52	97.2	99	This work
NiCu LDH	1.0 M KOH	10	1.45	1.65		91.2	[1]
CoCu	1.0M KOH	50	1.4	1.55	96	95	[2]
Ir-Co <sub>3</sub> O <sub>4</sub>	1.0 M KOH	50	1.45	1.42	98	98	[3]
NiCoP	1.0 M KOH	300	1.22	1.46		96.1	[4]
NiS <sub>x</sub> /Ni <sub>2</sub> P	1.0 M KOH	10	1.35	1.46		95.1	[5]
Co <sub>9</sub> S <sub>8</sub> -Ni <sub>3</sub> S <sub>2</sub>	1.0 M KOH	10	1.33	1.4	90	98.6	[6]
NiCo <sub>2</sub> O <sub>4</sub>	1.0 M KOH	10	1.35	1.45		99	[7]
NiCu NTs	1.0 M KOH	20	1.35	1.42	99	100	[8]
NiFeP	1.0 M KOH	10	1.37	1.44	99	94	[9]
NiOOH- Cu(OH) <sub>2</sub>	1.0 M NaOH	5		1.4	94.4	94.4	[10]

### References in Table S3.

- [1]. Zhang, J.; Yu, P.; Zeng, G.; Bao, F.; Yuan, Y.; & Huang, H. Boosting HMF Oxidation Performance Via Decorating Ultrathin Nickel Hydroxide Nanosheets with Amorphous Copper Hydroxide Islands. *J. Mater. Chem. A* **2021**, *9*, 9685-9691.
- [2]. Zhu, Y.; Shi, J.; Li, Y.; Lu, Y.; Zhou, B.; Wang, S.; & Zou, Y. Understanding the Surface Segregation Behavior of Bimetallic CoCu toward HMF Oxidation Reaction. *J. Energy Chem.* **2022**, *74*, 85-90.
- [3]. Lu, Y.; Liu, T.; Dong, C.; Huang, Y.; Li, Y.; Chen, J.; Zou, Y.; Wang, S. Tuning the Selective Adsorption Site of Biomass on Co<sub>3</sub>O<sub>4</sub> by Ir Single Atoms for Electrosynthesis. *Adv. Mater.* **2021**, *33*, 2007056.
- [4]. Wang, H.; Li, C.; An, J.; Zhuang, Y.; & Tao, S. Surface Reconstruction of NiCoP for Enhanced Biomass Upgrading. *J. Mater. Chem. A* **2021**, *9*, 18421-18430.
- [5]. Zhang, B.; Fu, H.; & Mu, T. Hierarchical NiS<sub>x</sub>/Ni<sub>2</sub>P Nanotube Arrays with Abundant Interfaces for Efficient Electrocatalytic Oxidation of 5-Hydroxymethylfurfural. *Green Chem.* **2022**, *24*, 877-884.
- [6]. Zhang, Y.; Xue, Z.; Zhao, X.; Zhang, B.; & Mu, T. Controllable and Facile Preparation of Co<sub>9</sub>S<sub>8</sub>-Ni<sub>3</sub>S<sub>2</sub> Heterostructures Embedded with N,S,O-tri-doped Carbon for Electrocatalytic Oxidation of 5-Hydroxymethylfurfural. *Green Chem.* **2022**, *24*, 1721-1731.

- [7]. Zhou, Z.; Xie, Y.-n.; Sun, L.; Wang, Z.; Wang, W.; Jiang, L.; Zhao, G. Strain-induced in Situ Formation of NiOOH Species on CoCo Bond for Selective Electrooxidation of 5-Hydroxymethylfurfural and Efficient Hydrogen Production. *Appl. Catal. B: Environ.* **2022**, *305*, 121072.
- [8]. Zheng, L.; Zhao, Y.; Xu, P.; Lv, Z.; Shi, X.; & Zheng, H. Biomass Upgrading Coupled with H<sub>2</sub> Production Via a Nonprecious and Versatile Cu-doped Nickel Nanotube Electrocatalyst. *J. Mater. Chem. A* **2022**, *10*, 10181-10191.
- [9]. Luo, R.; Li, Y.; Xing, L.; Wang, N.; Zhong, R.; Qian, Z.; Du, L. A Dynamic Ni(OH)<sub>2</sub>-NiOOH/NiFeP Heterojunction Enabling High-performance E-upgrading of Hydroxymethylfurfural. *Appl. Catal. B: Environ.* **2022**, *311*, 121357.
- [10]. Woo, J.; Moon, B. C.; Lee, U.; Oh, H.-S.; Chae, K. H.; Jun, Y.; Lee, D. K. Collaborative Electrochemical Oxidation of the Alcohol and Aldehyde Groups of 5-Hydroxymethylfurfural by NiOOH and Cu(OH)<sub>2</sub> for Superior 2,5-Furandicarboxylic Acid Production. *ACS Catal.* **2022**, *12*, 4078-4091.

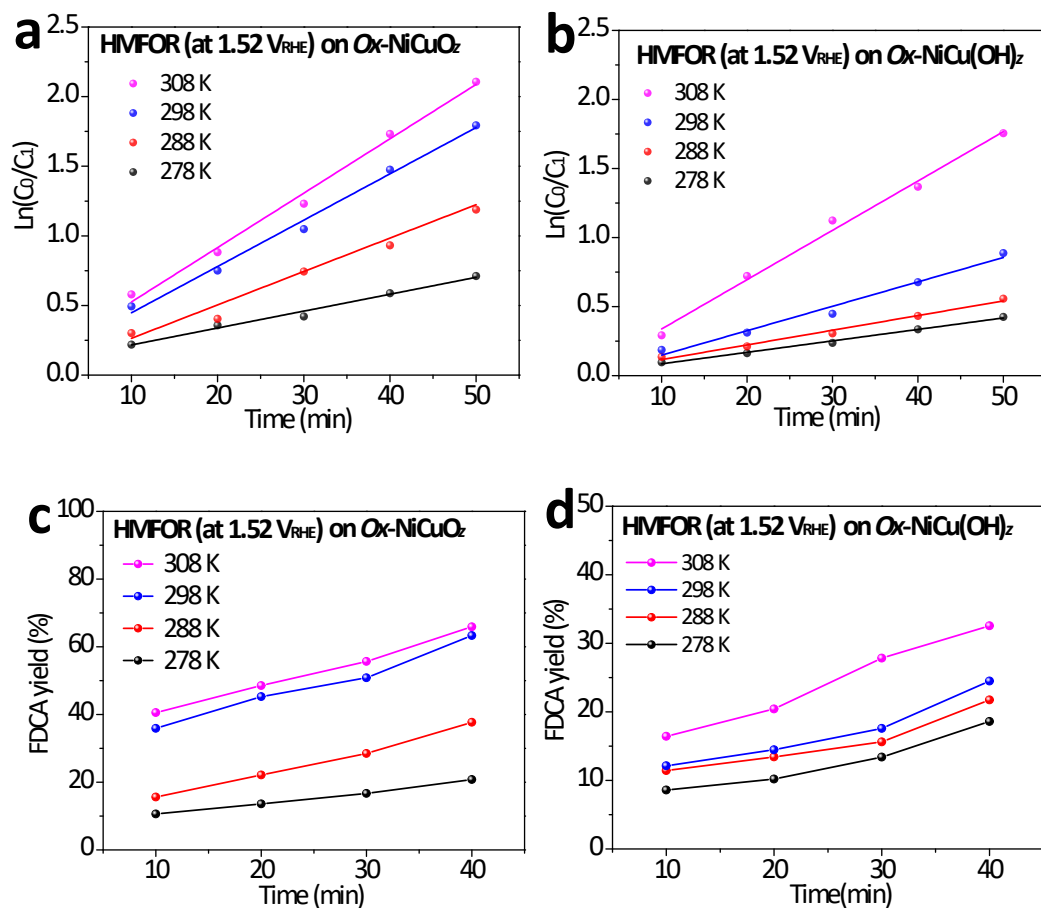


**Figure S25.** Time versus HFM conversion plots of CA tests over (a)  $O_x\text{-NiCuO}_z$  and (b)  $O_x\text{-NiCu(OH)}_z$  at  $1.52 V_{\text{RHE}}$  at various temperatures, and (c,d) corresponding FDCA yields.

Note: Arrhenius equation is as follows:  $k = Ae^{\frac{-E_a}{RT}}$

Where  $k$  is the rate constant,  $E_a$  is the apparent activation energy ( $\text{kJ mol}^{-1}$ ),  $A$  is the prefactor,  $R$  is the molar gas constant  $8.314 (\text{J}\cdot\text{mol}^{-1}\cdot\text{K}^{-1})$ ,  $T$  is the thermodynamic temperature (K).

Arrhenius equation could be transformed into the logarithm format:

$$\ln k = \frac{-E_a}{RT} + \ln A$$

It can be seen that a plot of  $\ln k$  against  $1/T$  should be a straight line with a slope of  $-E_a/R$ , based on which the  $E_a$  could be determined.

To estimate the  $E_a$  of HMFOR on  $O_x\text{-NiCuO}_z$  and  $O_x\text{-NiCu(OH)}_z$ , a single-pass HMFOR was conducted at  $1.52 V_{\text{RHE}}$  for 50 min at various temperatures (5, 15, 25 and 35 °C), and the HMF concentration ( $C_1$ ) was determined by HPLC every 10 min.

To estimate  $k$  of HMFOR at specific temperature,  $\ln(C_0/C_1)$  was plotted against

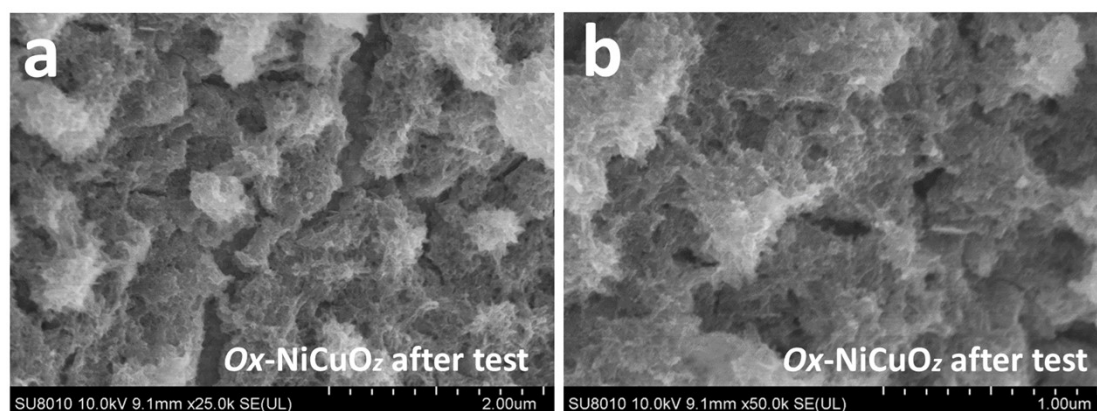
reaction time ( $t$ ) and the  $k$  was calculated based on the first-order kinetic equation of  $C = C_0 \exp(-kt)$ . Finally, the  $\ln k$  was plotted against  $1000/T$  and the  $E_a$  could be calculated based on the Arrhenius equation, as above mentioned.

To rationalize the above calculation, we also calculated and summarized the Faradaic efficiency (FE) of FDCA for the single-pass HMFOR on different catalysts (see **Table S4**). For  $Ox-NiCuO_z$ , the FE of FDCA is always higher than 90%, while that is always higher than 76% for  $Ox-NiCu(OH)_z$  in the employed temperature range. These results suggest that the oxidation of HMF to FDCA is the major reaction under our employed conditions. So, the calculated  $E_a$  values could roughly reflect the relative energy barriers of catalytic HMFOR towards FDCA, and hence the relative catalytic activities of different catalysts.

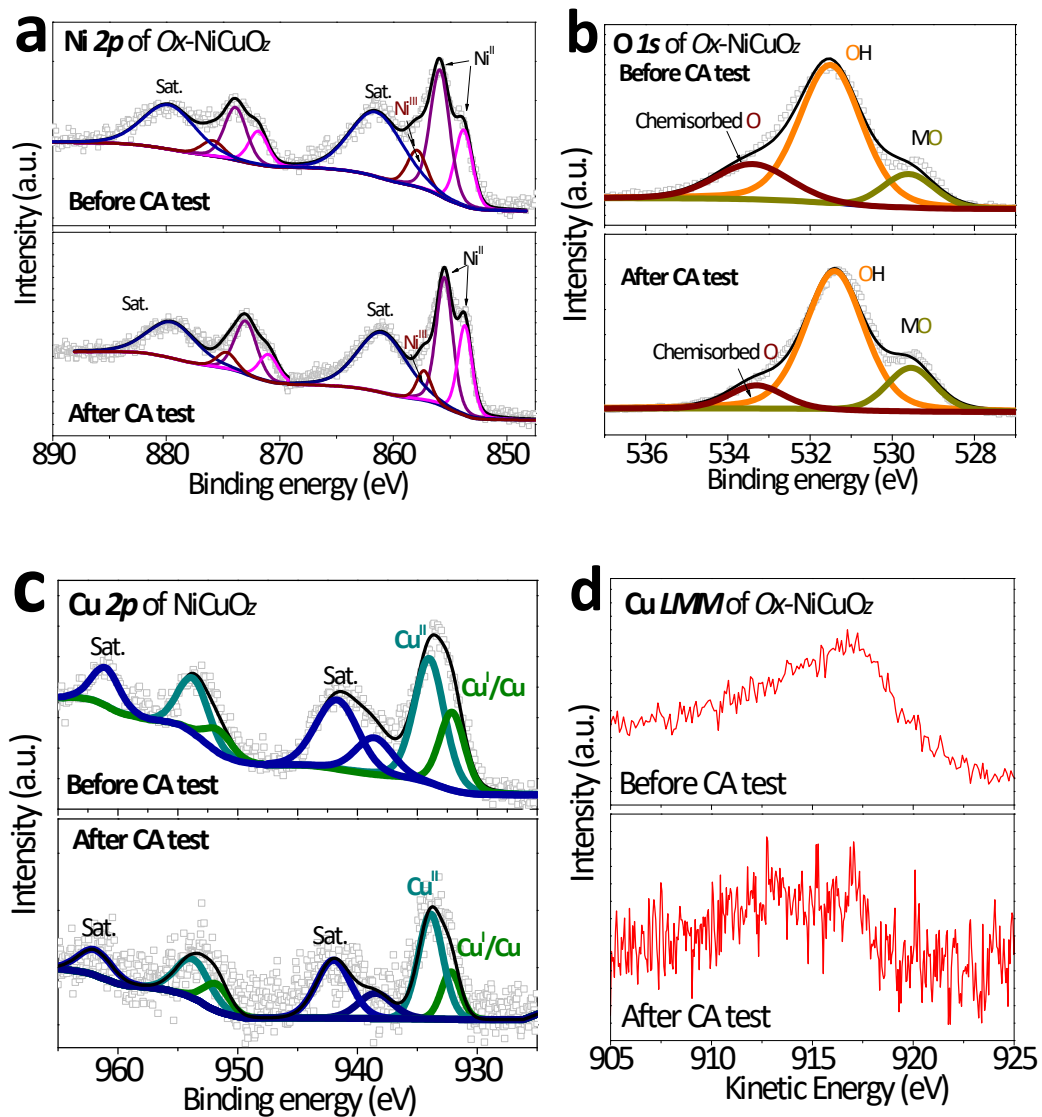
**Table S4.** Summary of the data measured and calculated for the single-pass HMFOR at varied temperature for 50 min on different catalyst.

Single-pass HMFOR on $Ox-NiCuO_z$ at 1.52 $V_{RHE}$ for 50 min						
Temp. (K)	HMF( $C_0$ ) <sup>a</sup> (mM)	HMF( $C_1$ ) <sup>a</sup> (mmol/L)	FDCA Yield (%)	Required charge for produced FDCA (C)	Actually passed charge (C)	FDCA FE (%)
278	10	4.91	30.50	98.88	101	97.9
288		3.05	48.60	157.56	160	98.5
298		1.66	77.40	250.92	255	98.4
308		1.22	80.57	261.20	287	91.0
Single-pass HMFOR on $Ox-NiCu(OH)_z$ at 1.52 $V_{RHE}$ for 50 min						
278	10	6.53	21.30	69.05	87	79.4
288		5.73	28.70	93.04	115	80.9
298		4.11	41.66	135.06	158	85.5
308		1.73	50.40	163.39	215	76.0

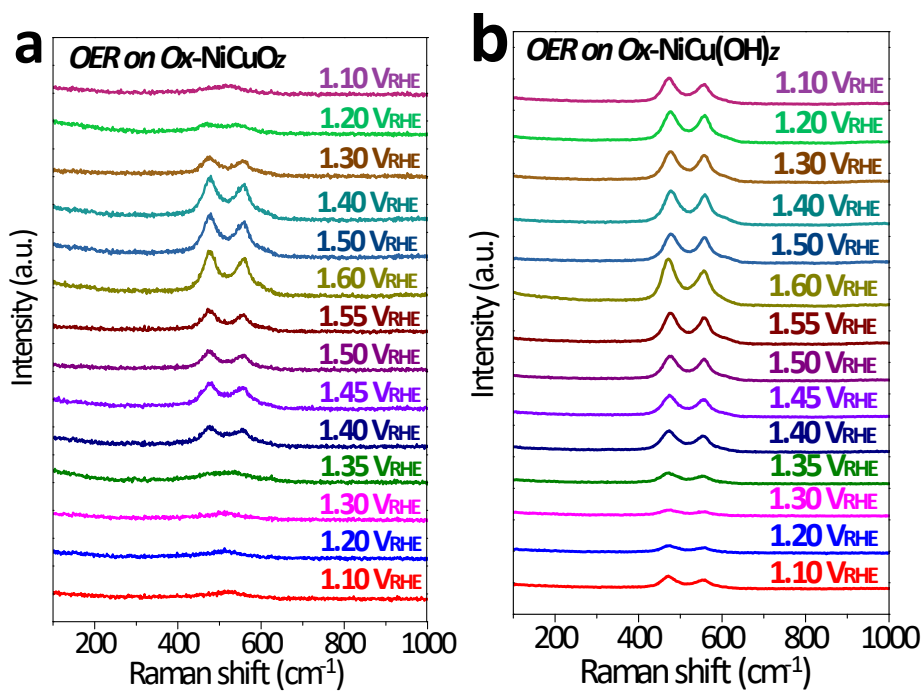
<sup>a</sup>  $C_0$  and  $C_1$  refer to the initial concentration of HMF and instantaneous concentration of remained HMF during the single-pass HMFOR.



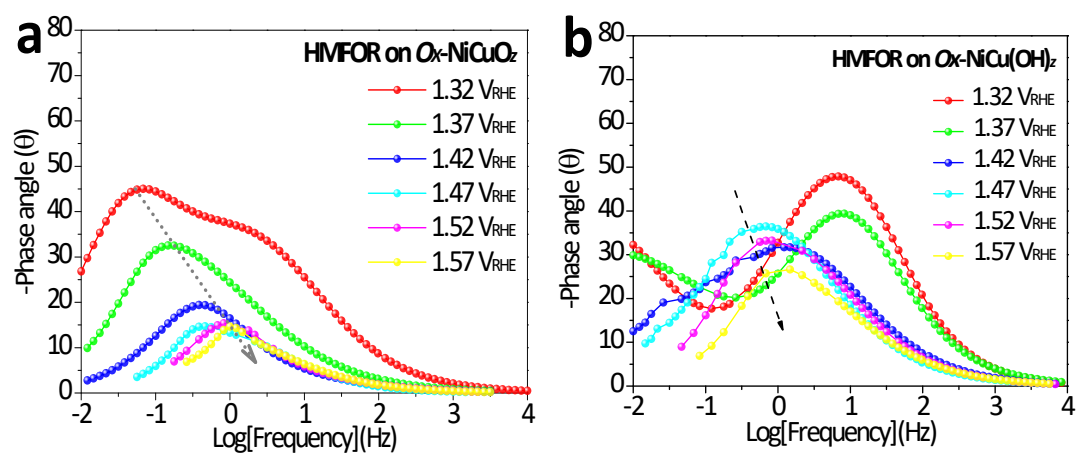
**Figure S26.** (a,b) SEM images of the  $Ox-NiCuO_z$  sample after the CA test at 1.52  $V_{RHE}$  under the HMFOR conditions.



**Figure S27.** Comparison between XPS spectra of the Ox-NiCuO<sub>2</sub> before and after the CA test at 1.52 V<sub>RHE</sub> under the HMFOR conditions: (a) Ni 2p, (b) O 1s, (c) Cu 2p, (d) Cu LMM.

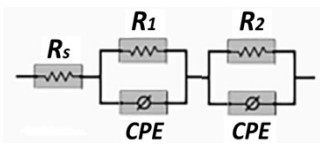


**Figure S28.** *In situ* Raman spectra of (a)  $Ox-NiCuO_z$  and (b)  $Ox-NiCu(OH)_z$  at different potentials under OER conditions.

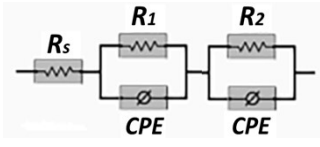


**Figure S29.** Bode plots of (a)  $Ox-NiCuO_z$  and (b)  $Ox-NiCu(OH)_z$  samples in 1 M KOH and 10 mM HMF.

**Table S5.** Analysis of impedance spectra of the HMFOR on  $Ox-NiCuO_z$  (1 M KOH/10 mM HMF)

	$R_s$ ( $\Omega$ )	$R_1$ ( $\Omega$ )	$R_2$ ( $\Omega$ )	Equivalent circuit
1.32	1.55	9.02	63.63	
1.37	1.55	6.38	4.27	
1.42	1.53	0.29	2.42	
1.47	1.53	0.37	1.43	
1.52	1.57	0.39	1.28	
1.57	1.60	0.40	0.99	

**Table S6.** Analysis of impedance spectra of the HMFOR on  $Ox-NiCu(OH)_z$  (1 M KOH/10 mM HMF)

	$R_s$ ( $\Omega$ )	$R_1$ ( $\Omega$ )	$R_2$ ( $\Omega$ )	Equivalent circuit
1.32	2.08	31.60	336.20	
1.37	2.04	13.35	216.70	
1.42	2.07	12.48	15.21	
1.47	2.06	10.60	12.22	
1.52	2.04	8.84	6.11	
1.57	2.07	4.62	3.29	

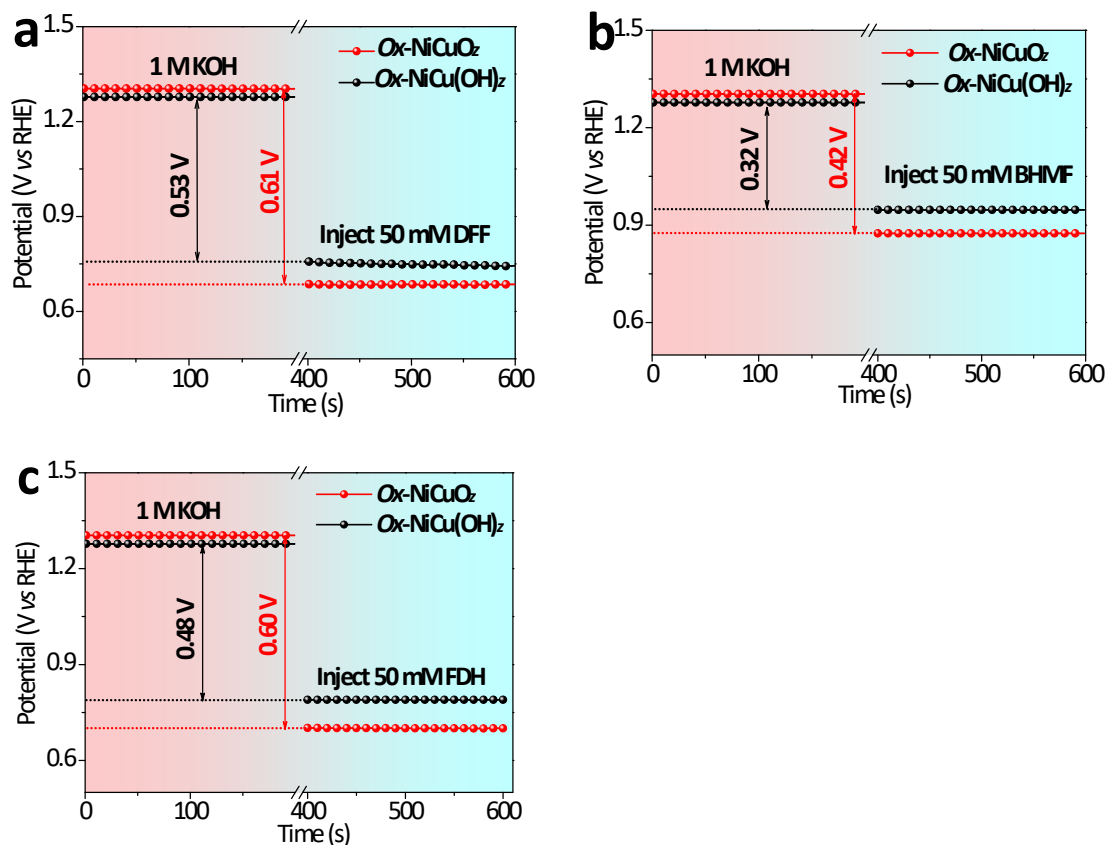


**Figure S30.** OCP profiles of  $Ox-NiCuO_2$  and  $Ox-NiCu(OH)_2$  in 1 M KOH with 50 mM (a) DFF, (b) BHMf and (c) FDH injected after 150 s.

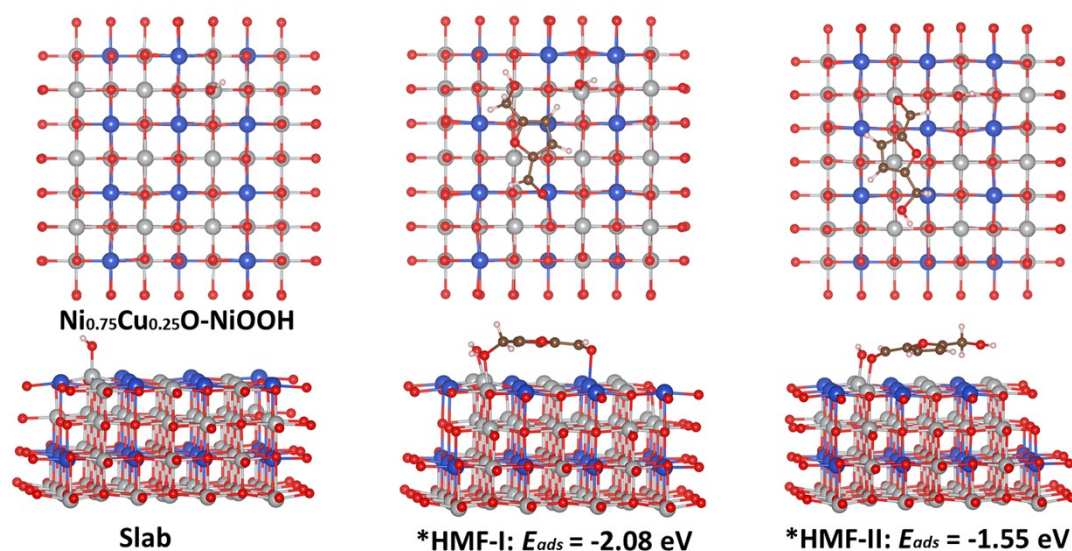


**Figure S31.** DFT optimized  $Ni_{0.75}Cu_{0.25}O$  with a  $Ni^{III}OOH$  species and those models each with an adsorbed HMF in different orientations (\*HMF-I: the adsorbed HMF close to  $Ni^{III}OOH$  by  $-OH$  group; \*HMF-II: the adsorbed HMF close to  $Ni^{III}OOH$  by  $-CHO$  group).



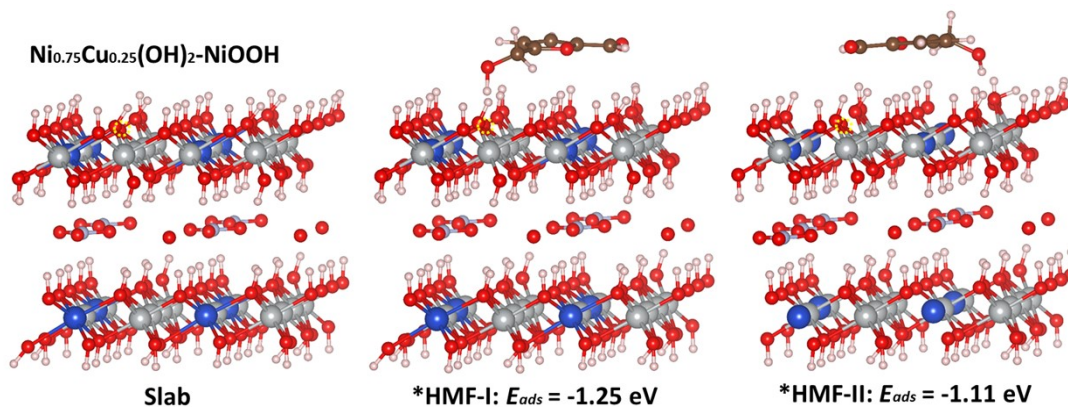


**Figure S32.** DFT optimized Ni<sub>0.75</sub>Cu<sub>0.25</sub>(OH)<sub>2</sub> with a Ni<sup>III</sup>OOH species and those models each with an adsorbed HMF in different orientations (\*HMF-I: the adsorbed HMF close to Ni<sup>III</sup>(OH)O by –OH group; \*HMF-II: the adsorbed HMF close to Ni<sup>III</sup>(OH)O by –CHO group). The yellow circle indicates the electrophilic oxygen of Ni<sup>III</sup>OOH.

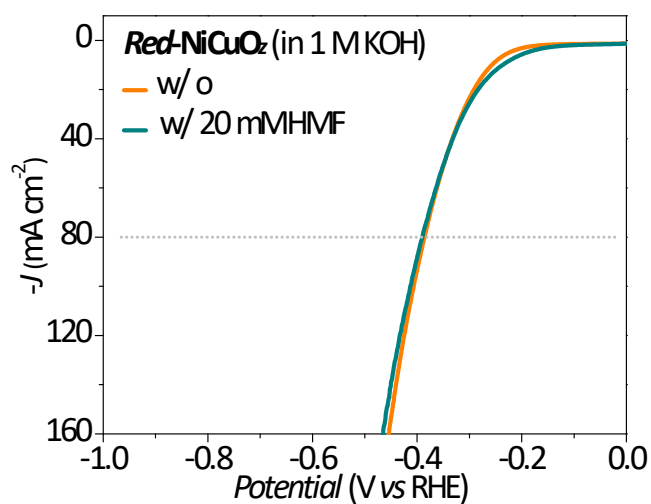


**Figure S33.** LSV curves (with 95%  $iR$  compensation) of Red-NiCuO<sub>2</sub> in 1 M KOH without/with 20 mM HMF.

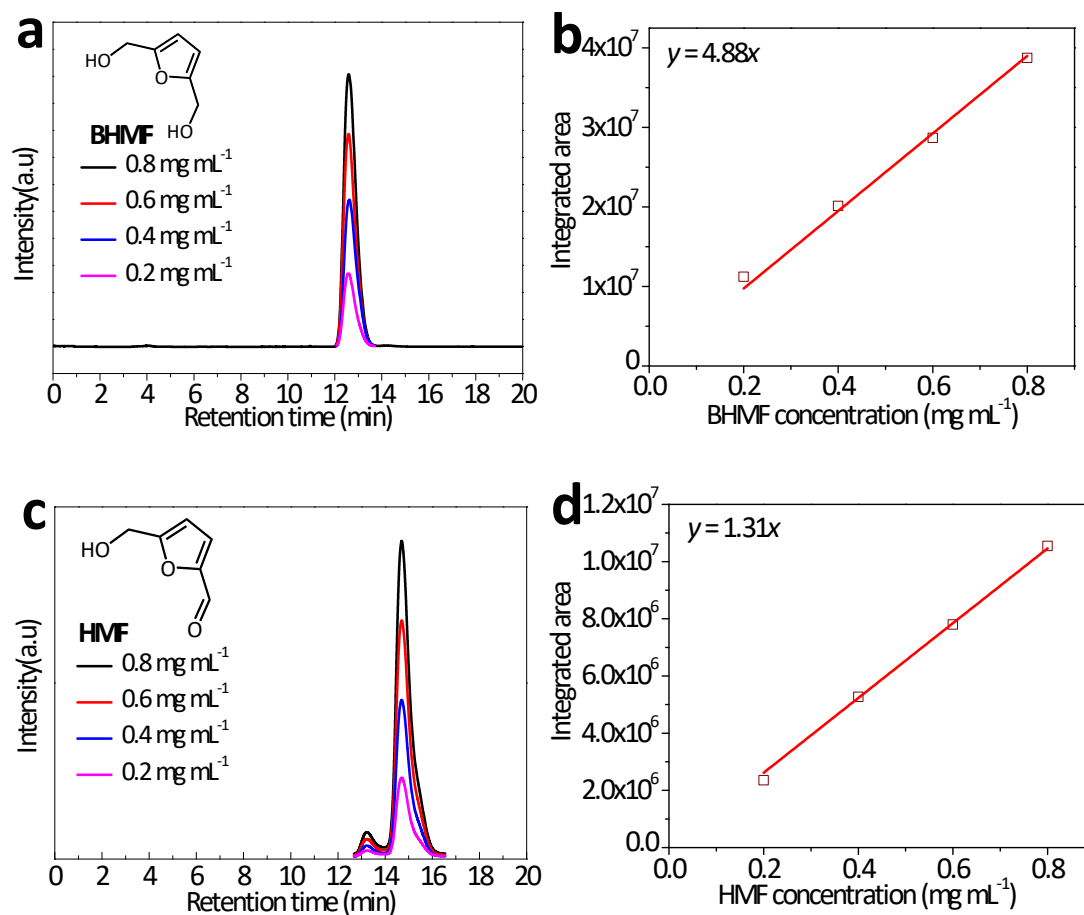


**Figure S34.** HPLC chromatograms (with a detector of  $\lambda = 220$  nm) and calibration plots of standard samples of (a,b) BHMF, (c,d) HMF.

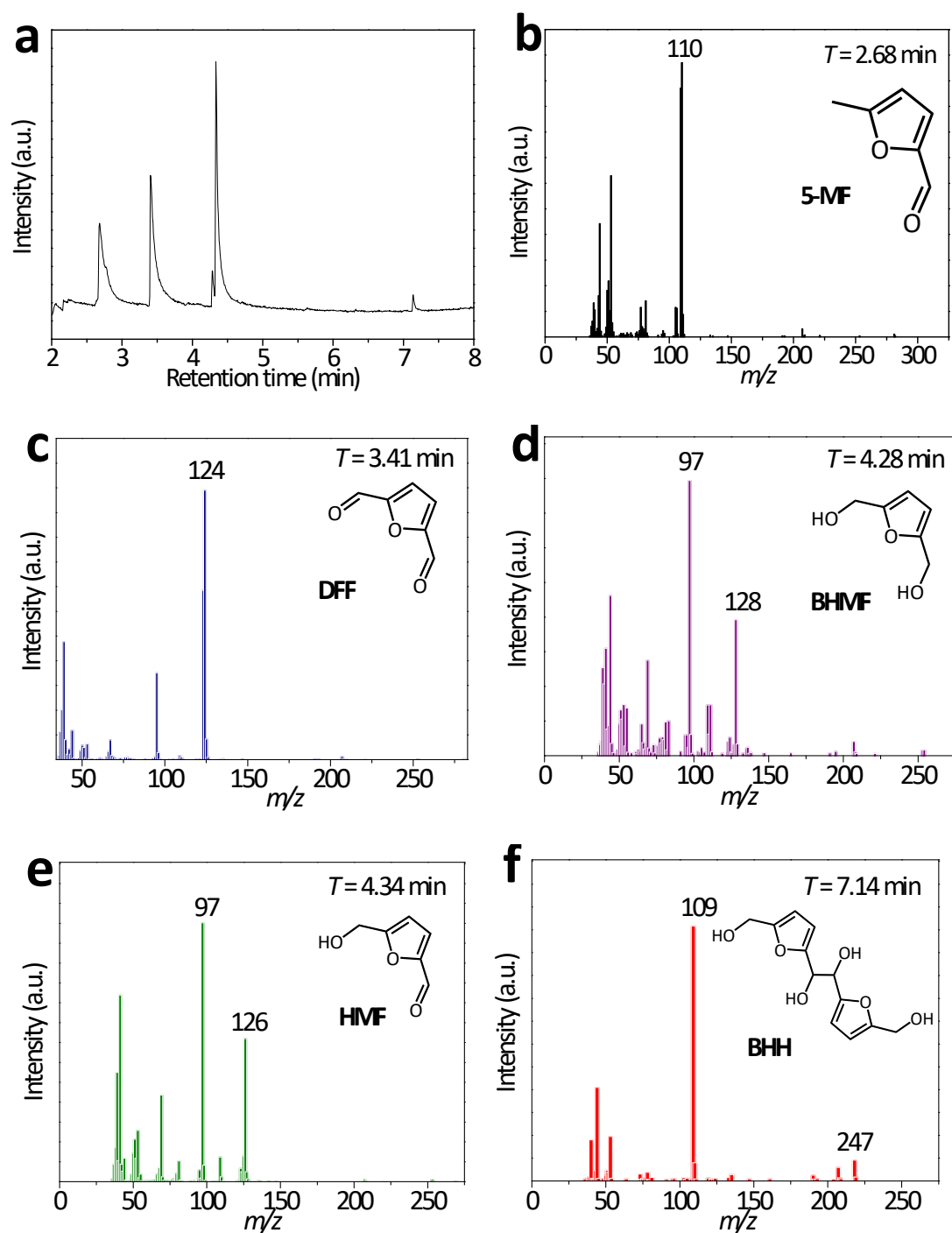


**Figure S35.** (a) Gas chromatogram of extracted products of HMFRR at  $-0.7 V_{\text{RHE}}$ , and (b-f) mass analysis results. The results suggest the possible products of 5-methylfurfuryl aldehyde (5-MF), 2,5-diformylfuran (DFF), 2,5-bishydroxymethylfuran (BHMF) and 5,5'-bis(hydroxymethyl)hydrofuroin (BHH).

Note: To prepare the sample for gas chromatogram mass analysis, 9 mL ethyl acetate was used to extract the HMFRR products from 3 mL electrolyte. After the separation and drying, the extract was filtered for analysis.

Note: The product DFF might be due to the self-oxidation of HMF in presence of air.

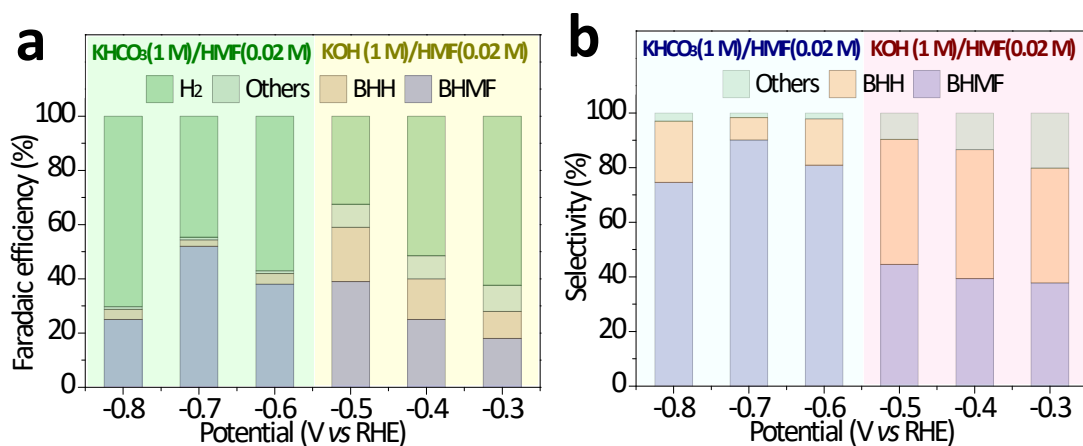


**Figure S36.** Potential-dependent FE and selectivity of BHMf for HMFRR (each with passed charge of 50 C) in (a) 1 M KHCO<sub>3</sub> and (b) 1 M KOH without/with 20 mM HMF.

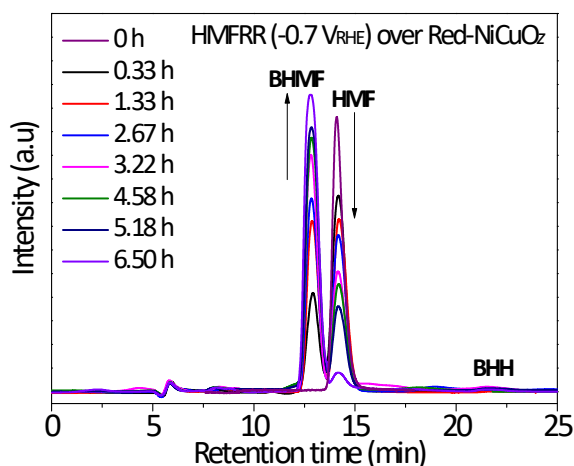


**Figure S37.** HPLC chromatograms (with a monitor of  $\lambda = 220$  nm) of HMFRR products at  $-0.7$  V<sub>RHE</sub> over Red-NiCuO<sub>2</sub> with the increasing of reaction time.

Note: As the standard sample of BHH is not commercially available, it is usually supposed that the absorbance of BHH at  $\lambda = 220$  nm is two-fold that of BHMf.<sup>1</sup>

Reference in Note of **Figure S37**.

[1] K. Ji, M. Xu, S.-M. Xu, Y. Wang, R. Ge, X. Hu, X. Sun, .H. Duan, Electrocatalytic Hydrogenation of 5-Hydroxymethylfurfural Promoted by a Ru1Cu Single-Atom Alloy Catalyst. *Angew. Chem. Int. Ed.* **2022**, *61*, e202209849.

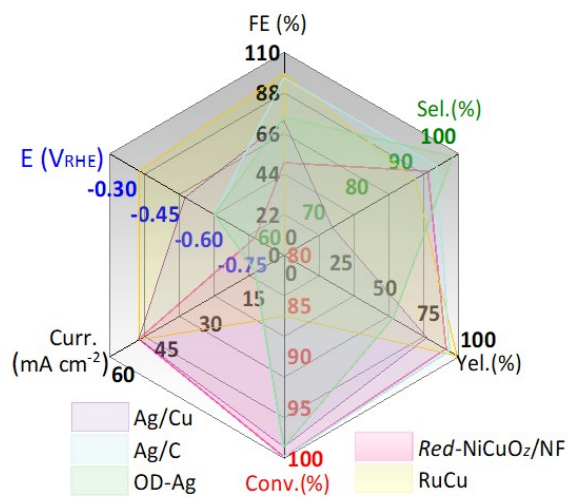


**Figure S38.** Comparison of state-of-the-art performance of recently reported catalysts towards HMFRR.

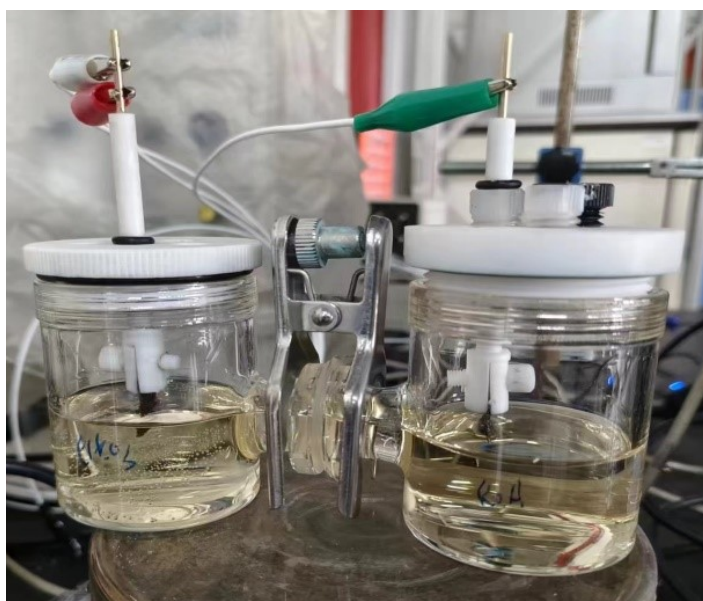


**Figure S39.** Photo of a two-electrode system for HMFRR/HMFOR electrolysis.

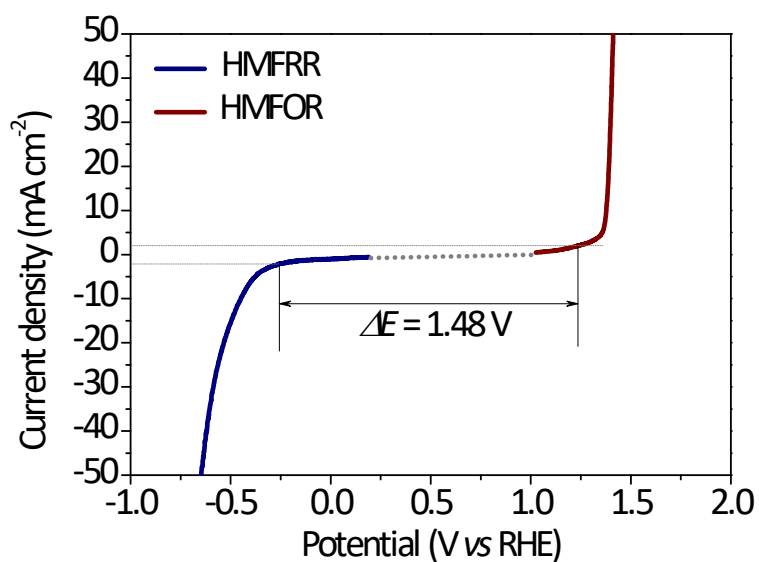


**Figure S40.** Combined LSV curves of *Ox*-NiCuO<sub>2</sub> and *Red*-NiCuO<sub>2</sub> towards HMFOR (1 M KOH with 10 mM HMF) and HMFRR (1 M KHCO<sub>3</sub> with 20 mM HMF), respectively, each recorded with a three-electrode system.

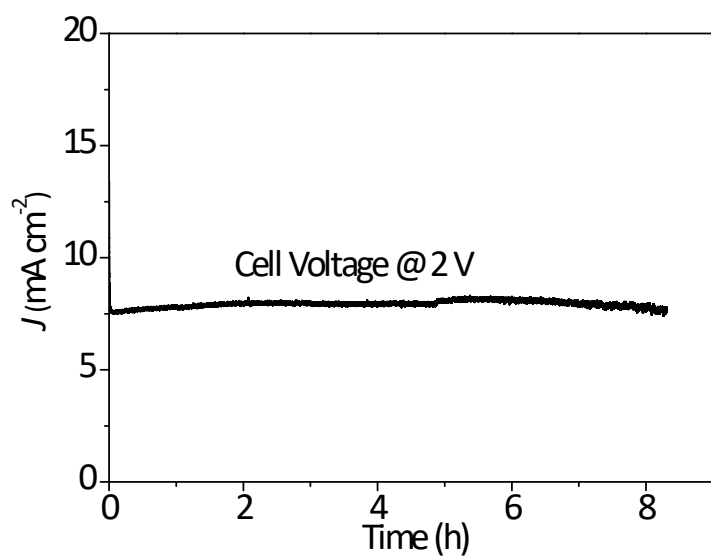


**Figure S41.** Chronoamperometry (CA) profile of *Red*-NiCuO<sub>2</sub>//*Ox*-NiCuO<sub>2</sub> towards HMFRR/HMFOR electrolysis at 2.0 V for 8 h.

**Table S7.** Summary of catalytic performance of electrocatalysts towards HMFRR.

Catalyst	Electrolyte	Initial HMF (mM)	Potential (V vs RHE)	BHMF sel (%)	BHMF yield (%)	FE (%)	Ref.
<i>Red</i> -NiCuO <sub>2</sub>	1.0 M KHCO <sub>3</sub>	20	-0.7	90	97.5	56	This work
BiSn	0.5 M borate buffer	20	-0.4		77	100	[1]
AgCu	0.5 M borate buffer	20	-1.3 vs SCE	87	80	100	[2]
OD Ag	0.5 M borate buffer	20	-0.6	98.2	62.7		[3]
Ag NPs/CC	0.5 M borate buffer	100	-0.7	75.5	48.4		[4]
Ag	0.5 M borate buffer	20	-0.5		60.9		[5]

**References in Table S7.**

- [1]. Piao, G.; Yoon, S. H.; Cha, H. G.; Han, D. S.; & Park, H. Porous Dendritic BiSn Electrocatalysts for Hydrogenation of 5-Hydroxymethylfurfural. *J. Mater. Chem. A* **2022**, *10*, 24006-24017.
- [2]. Sanghez de Luna, G.; Ho, P. H.; Sacco, A.; Hernández, S.; Velasco-Vélez, J.-J.; Ospitali, F.; Benito, P. AgCu Bimetallic Electrocatalysts for the Reduction of Biomass-Derived Compounds. *ACS Appl. Mater. Interfaces* **2021**, *13*, 23675-23688.
- [3]. Liu, H.; Lee, T.-H.; Chen, Y.; Cochran, E. W.; & Li, W. Paired Electrolysis of 5-(hydroxymethyl)furfural in Flow Cells with a High-performance Oxide-derived Silver Cathode. *Green Chem.* **2021**, *23*, 5056-5063.
- [4]. Liu, H.; Lee, T.-H.; Chen, Y.; Cochran, E. W.; & Li, W. Paired and Tandem Electrochemical Conversion of 5-(Hydroxymethyl)furfural Using Membrane-Electrode Assembly-Based Electrolytic Systems. *ChemElectroChem* **2021**, *8*, 2817-2824.
- [5]. Lee, D. K.; Kubota, S. R.; Janes, A. N.; Bender, M. T.; Woo, J.; Schmidt, J. R.; & Choi, K.-S. The Impact of 5-Hydroxymethylfurfural (HMF)-Metal Interactions on the Electrochemical Reduction Pathways of HMF on Various Metal Electrodes. *ChemSusChem* **2021**, *14*, 4563-4572.

**Table S8.** Summary of paired electrolysis of HMFRR/HMFOR.

HMF (mM)	Electrolyte	Reactor	Cathode	Anode	Cell-voltage	Combined FE (%)	Ref.
10/10	0.5 M borate buffer (pH 9.2)	H-cell	Ag/C	Carbon felt (TEMPO mediated)	-1.3 V	85/98	[1]
10/10	0.2 M HClO <sub>4</sub>	Flow cell	Pd/VN	3D VN	2.5 -3.0 V	≥86/≥84	[2]
20/20	0.5 M borate buffer (pH 9.2)	Flow cell	OD-Ag	Carbon cloth (TEMPOmediated)	2.0 V	80.9/83.4	[3]
20/10	1 M KHCO <sub>3</sub> /1 M KOH	H-cell	Red-NiCuOz	Ox-NiCuOz	2.0 V	Nearly 150%	This work

**References in Table S8.**

- [1]. Chadderdon, X. H.; Chadderdon, D. J.; Pfennig, T.; Shanks, B. H.; & Li, W. Paired Electrocatalytic Hydrogenation and Oxidation of 5-(Hydroxymethyl)furfural for Efficient Production of Biomass-derived Monomers. *Green Chem.* **2019**, *21*, 6210-6219.
- [2]. Sui, L.; Xiang, S.; Yao, Z.; Zhong, X.; Yong, C.; Yu, L.; Zhong, W.; & Jiang, W.; Biomass Valorization via Paired Electrosynthesis Over Vanadium Nitride-Based Electrocatalysts. *Adv. Funct. Mater.* **2019**, *29*, 1904780.
- [3]. Liu, H.; Lee, T.-H.; Chen, Y.; Cochran, E. W.; & Li, W. Paired Electrolysis of 5-(hydroxymethyl)furfural in Flow Cells with a High-performance Oxide-derived Silver Cathode. *Green Chem.* **2021**, *23*, 5056-5063.